

The importance of being empty: a spectral approach to Hopfield neural networks with diluted examples

Elena Agliari,^{a,1} Alberto Fachechi,^{a,1} Domenico Luongo^b

^a*Department of Mathematics G. Castelnuovo, Sapienza Università di Roma, Italy*

^b*Scuola Normale Superiore, Pisa, Italy*

¹*GNFM-INdAM, Gruppo Nazionale di Fisica Matematica (Istituto Nazionale di Alta Matematica), Italy*

E-mail: agliari@mat.uniroma1.it

ABSTRACT: We consider Hopfield networks, where neurons interact pair-wise by Hebbian couplings built over *i.* a set of definite patterns (ground truths), *ii.* a sample of labeled examples (supervised setting), *iii.* a sample of unlabeled examples (unsupervised setting). We focus on the case where ground-truths are Rademacher vectors and examples are noisy versions of these ground-truths, possibly displaying some blank entries (e.g., mimicking missing or dropped data), and we determine the spectral distribution of the coupling matrices in the three scenarios, by exploiting and extending the Marchenko-Pastur theorem. By leveraging this knowledge, we are able to analytically inspect the stability and attractiveness of the ground truths, as well as the generalization capabilities of the networks. In particular, as corroborated by long-running Monte Carlo simulations, the presence of blank entries can have benefits in some specific conditions, suggesting strategies based on data sparsification; the robustness of these results in structured datasets is confirmed numerically. Finally, we demonstrate that the Hebbian matrix, built on sparse examples, can be recovered as the fixed point of a gradient descent algorithm with dropout, over a suitable loss function.

Contents

1	Introduction	2
2	Setting and definitions	3
2.1	Attractor neural networks	3
2.2	Introducing the setting: ground-truths, synthetic datasets and dilution	4
3	Spectra of coupling matrices	6
4	Validity of the models with examples: squared error	8
5	1-step stability, attractiveness and capacity of generalization	9
6	Numerical simulations for the unsupervised setting	16
6.1	An experiment with a structured dataset	21
7	Discussion and outlooks	23
A	Linking dropout and diluted datasets: a Machine Learning perspective	24
B	Proofs	26
B.1	Proof of Prop. 1	26
B.2	Proof of Prop. 3	26
B.3	Proof of Prop. 4	28
C	The Approximate Factorization Method	30
C.1	The $M \rightarrow \infty$ limit	31
C.2	Finite (but large) M : the Approximate Factorization Method	32
C.3	A counterexample at finite (but small) M	33
C.4	An algebraic comment on AFM	34
C.5	Time to face the reality: simulations	35
D	Frobenius norm and squared error	35
D.1	Γ^s vs Γ : the validity of supervised Hebb's rule	37
D.2	Γ^u vs Γ : the validity of unsupervised Hebb's rule	38
E	A comparison with signal-to-noise analysis	39

1 Introduction

In the last decades, science and technology have been revolutionized by the advent of modern Artificial Intelligence (AI), whose success is mainly due to the availability of big data at small cost as well as the high computational capabilities of parallel processing systems. This very success, however, poses significant challenges in implementing Machine Learning models able to accomplish the desired tasks, especially given the typical size of benchmark datasets and the extreme complexity of modern AI solutions. In particular, several strategies have been investigated in the literature in order to reduce the sensitivity of the generalization power of data-driven decision-making systems and high-complexity neural networks on the quality of training data. These strategies aim to optimize the performances of such models through approaches such as data cleaning and augmentation [1–3], the usage of specific cost-functions [4, 5] or algorithms [6], regularization, dropout and noise injection [7–9], or more sophisticated methods and training procedures [10–12]. Nevertheless, while investigations in this direction are undoubtedly crucial, they are often rather empirical in nature, and in practical applications an extensive fine-tuning of parameters is often required. In fact, a comprehensive and well-controllable theoretical framework, equipped with rigorous mathematical techniques, for interpreting their working principle is still under construction.

Recently, the Hopfield model – a prototypical energy-based neural network – has been revised [13–18] and consistently analyzed to address the emergence of generalization in a simplified but solid-grounded setting (see also [19–21]). In particular, in [22] an unsupervised reconstruction task of hidden patterns with a L_2 -regularized loss function has been mapped to Hopfield-like neural networks [23], with the regularization parameter playing the role of *dreaming time* shaping the attraction basins of stored vectors. Consequently, the emergence of the generalization phase can be interpreted as the result of the coalescence of attraction basins associated to training examples, while overfitting occurs for choices of the regularization parameters resolving them. In this paper, we advance this investigation, focusing on the effect of missing data on the retrieval and generalization capabilities of such networks. The absence of some data entries is assumed as completely random, that is, the probability of missingness is independent of both observed and unobserved variables (this might occur, for instance, when a sensor fails randomly during data collection, or can be made *a posteriori* as in dropout-like techniques [8]). Specifically, we consider the following framework: we have a set of K *patterns*, each corresponding to a different ground-truth feature, represented by a binary vector of length N and denoted as $\xi^\mu \in \{-1, +1\}^N$, for $\mu = 1, \dots, K$. The available dataset comprises M different measurements of these features, denoted as $\xi^{\mu,A}$, for $\mu = 1, \dots, K$ and $A = 1, \dots, M$. These measurements are affected by a random error, meaning that some entries can be flipped, namely $\xi_i^{\mu,A} = -\xi_i^\mu$ or can be missing, namely $\xi_i^{\mu,A} = 0$, for some i, μ, A , and are combined into the Hebbian matrix. Following [24–26], we envisage two ways to build up the Hebbian matrix, that mirror, respectively a supervised and unsupervised protocol yielding to the coupling matrices Γ^s and Γ^u ; in the first setting, knowledge of class partitioning of the examples is used to approximate the unknown μ -th pattern through the empirical average of the examples belonging to the μ -th class, and these averages $\bar{\xi}^\mu$ are then stored in the Hebbian matrix: $\Gamma_{i,j}^s \propto \sum_\mu \bar{\xi}_i^\mu \bar{\xi}_j^\mu$; conversely, in the unsupervised scenario, such knowledge is unavailable, thus single entries are all combined in the coupling matrix as $\Gamma_{i,j}^u \propto \sum_{\mu,A} \xi_i^{\mu,A} \xi_j^{\mu,A}$, so that each training example enters in the energetic landscape with its own attraction basin. As a first result, we analytically inspect the algebraic properties of these matrices, obtaining their spectral distribution, by which we can estimate their normalized Frobenius distance with respect to the ground-truth Hebbian matrix. By interpreting this distance as an error affecting the experimental matrices, we find that this increases sigmoidally with the fraction of flipped entries,

and sparseness has a more negative impact in the unsupervised scenario. Further, we are able to assess the generalization capabilities of the models in terms of the first and second moments of the spectral distributions of the coupling matrices; this approach is also shown to encompass the popular signal-to-noise analysis. In this way, we are able to analytically highlight that, in the supervised case, dilution always impairs the generalization capabilities, with a stronger effect when the initial datum is farther from the target; conversely, in the unsupervised case, our theoretical results suggest that dilution can enhance performance as long as the quality of data points is relatively high and the load K/N is relatively large. Remarkably, these predictions are confirmed by Monte Carlo simulations in the random setting and for structured datasets. This supports the claim that the beneficial effect of dilution is a general phenomenon occurring in attractor neural networks with coupling matrix built with empirical data, leading to better-performing models in terms of generalization capabilities and suggesting the possible development of targeted dropout strategies.

The paper is organized as follows. In Sec. 2 we present the model and the datasets, distinguishing between basic storing, supervised and unsupervised protocols. Next, in Sec. 3 we apply the Marchenko-Pastur theorem to determine the spectra of the related coupling matrices, namely $\mathbf{\Gamma}$, $\mathbf{\Gamma}^s$, and $\mathbf{\Gamma}^u$, respectively. These results will be employed in Sec. 4 to get analytical estimates on the squared error implied by replacing the ideal coupling matrix $\mathbf{\Gamma}$ with its experimental realizations $\mathbf{\Gamma}^s$, and $\mathbf{\Gamma}^u$, and in Sec. 5 to analytically inspect the stability and attractiveness of the ground truths, as well as the generalization capabilities of the networks. The non-trivial findings concerning the generalization capabilities in the unsupervised setting are further inspected numerically in Sec. 6, where the benefits of sparsification in the training data is assessed. Finally, Sec. 7 contains our conclusions and outlooks. Lengthy proofs of theorems and technical details are collected in the Appendices.

2 Setting and definitions

2.1 Attractor neural networks

We consider a fully-connected associative neural network (ANN) made of N binary neurons whose state is denoted by a binary variable $\sigma_i \in \{-1, +1\}$ for $i = 1, \dots, N$; the overall neural configuration is represented by the vector $\boldsymbol{\sigma} = (\sigma_1, \dots, \sigma_N) \in \{-1, +1\}^N$. In general, $\boldsymbol{\sigma}$ is a dynamic variable and it is iteratively updated according to the *parallel* evolution rule, also referred to as Glauber dynamics,

$$\boldsymbol{\sigma}^{(n+1)} = \text{sgn}(\mathbf{J} \cdot \boldsymbol{\sigma}^{(n)}), \quad (2.1)$$

where the superscript n counts the number of updating steps and \mathbf{J} is a $N \times N$ real matrix encoding the synaptic efficiencies. The previous equation is equivalent to say that each single neuron at the $(n+1)$ -th step takes the value $\sigma_i^{(n+1)} = \text{sgn}(\sum_j J_{i,j} \sigma_j^{(n)})$. The matrix entry $J_{i,j}$ therefore represents the strength by which the j -th neuron influences the state of the i -th neuron. This iterative updating is visualized in Fig. 1 in terms of a multi-layered network, where the n -th layer encodes for the configuration $\boldsymbol{\sigma}^{(n)}$ and the information propagates from one layer to the next according to the rule (2.1). Specifically, $\boldsymbol{\sigma}^{(0)}$ is interpreted as the *input* of our neural network, and we are interested in the related output $\boldsymbol{\sigma}^{(T)}$ for some large T (*vide infra*) or, more precisely, in the input-output mapping performed by the machine. To this purpose, it is worth recalling that (see e.g., [27, 28]), if \mathbf{J} is a symmetric matrix with non-negative diagonal entries (i.e. $J_{i,j} = J_{j,i} \forall i, j$ and $J_{i,i} \geq 0$), the dynamics described in eq. (2.1) admits the bounded Lyapunov function $L(\boldsymbol{\sigma}) = -\sum_i |\sum_j J_{i,j} \sigma_j|$, which implies that the dynamics converges to a fixed point, i.e. a configuration invariant under the dynamics (2.1), or to a period-2

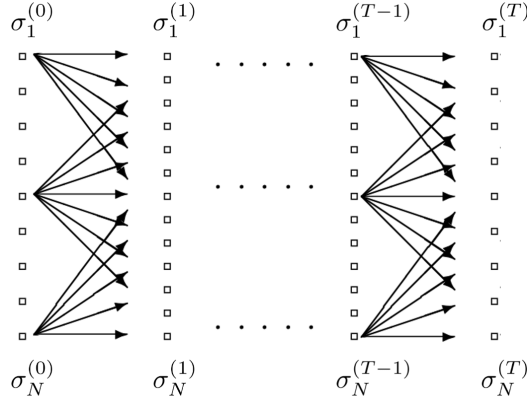


Figure 1. Schematic representation of an associative neural network as a multilayer neural network.

limit cycle, namely $\exists \tilde{T} > 0$ s.t. $\forall n \geq \tilde{T} \quad \sigma^{(n)} = \sigma^{(n+2)}$. As a consequence, whether the dynamics converges to a fixed point $\sigma^{(\infty)} := \lim_{n \rightarrow \infty} \sigma^{(n)}$, we will interpret it as the *output* of the ANN.

2.2 Introducing the setting: ground-truths, synthetic datasets and dilution

Let us suppose to have K patterns of information, also referred to as *archetypes* or *ground-truths*, codified by binary vectors of length N and denoted by $\xi^\mu = (\xi_1^\mu, \dots, \xi_N^\mu) \in \{-1, +1\}^N$, $\mu = 1, \dots, K$. This is the information that we want to retrieve and we state that a pattern, say ξ^μ , is retrievable by the network if the configuration $\sigma = \xi^\mu$ is a fixed point for the dynamics (2.1), with a finite attraction basin \mathcal{B}_μ . The configurations belonging to the attraction basin \mathcal{B}_μ are interpreted as input configurations that prompt the retrieval of the pattern ξ^μ . Thus, the larger the cardinality $|\mathcal{B}_\mu|$ and the more attractive the pattern ξ^μ is. On the other hand, if $|\mathcal{B}_\mu| = 1$, ξ^μ is an unstable fixed point, which is useless for retrieval purposes. We also introduce the *load*, defined as $\alpha_N := K/N$, representing the amount of information that we aim to store in the network, given a certain amount of resources (i.e., of neurons). In the limit of large N , we distinguish between the so-called “high-storage” regime, where $(0, \infty) \ni \alpha := \lim_{N \rightarrow \infty} \alpha_N$ and the so-called “low-storage” regime, where $\alpha = 0$; in the following we will focus on the former.

As far as the statistical properties of patterns are concerned, we will conduct our analysis under a controllable setting, that is, we will assume that $\{\xi_i^\mu\}_{\mu,i}$ is a class of i.i.d. random variables, with symmetric Rademacher distribution $Rad(0)$, thus:

$$\mathcal{P}(\xi_i^\mu) = \frac{1}{2}(\delta_{\xi_i^\mu, +1} + \delta_{\xi_i^\mu, -1}). \quad (2.2)$$

Recalling (2.1), we notice that, in order for each of the patterns ξ to be a fixed point, the interaction matrix \mathbf{J} must be a function of the whole set of patterns. A standard choice is provided by the

following¹

$$\Gamma_{i,j} = \frac{1}{N} \sum_{\mu=1}^K \xi_i^\mu \xi_j^\mu, \quad \forall i, j \in \{1, \dots, N\}, \quad (2.3)$$

which can be rewritten in matrix form as $\mathbf{\Gamma} = N^{-1} \mathbf{X} \mathbf{X}^T$, where \mathbf{X} is a $N \times K$ matrix, with entries $X_{i,\mu} = \xi_i^\mu$, $\forall i \in \{1, \dots, N\}$, $\forall \mu \in \{1, \dots, K\}$. This choice for \mathbf{J} is inspired by the empirical Hebb's rule [34, 35], and, as proved in [36], ensures the retrieval up to a load $\alpha \approx 0.138$ at zero temperature. This framework, where the information to be retrieved is fully and perfectly accessible, represents an ideal setting, which we refer to as **basic storing**.

In real applications, we expect to be able to rely only on experimental, noisy realizations of archetypes, that we call *examples*. In order to have mathematical control, we define $M \in \mathbb{N}^+$ synthetic examples $\{\boldsymbol{\xi}^{\mu,A}\}_{A=1,\dots,M}$ for each archetype $\boldsymbol{\xi}^\mu$, as $\xi_i^{\mu,A} = \xi_i^\mu \chi_i^{\mu,A}$, with $i \in \{1, \dots, N\}$, $\mu \in \{1, \dots, K\}$, and $A \in \{1, \dots, M\}$, and where $\chi_i^{\mu,A}$ encodes the *error* in the i -th bit of the A -th example related to the μ -th class. The $\{\chi_i^{\mu,A}\}_{\mu,A,i}$ are modeled as i.i.d. random variables, independent of the archetypes $\boldsymbol{\xi}^\mu$ s, with probability

$$\mathcal{P}(\chi_i^{\mu,A}) = (1-d) \frac{1+r}{2} \delta_{\chi_i^{\mu,A}, +1} + (1-d) \frac{1-r}{2} \delta_{\chi_i^{\mu,A}, -1} + d \delta_{\chi_i^{\mu,A}, 0}. \quad (2.4)$$

Thus, $d \in (0, 1)$ is the probability that the entry of any given example is 0 and this is interpreted as a missing datum; in other words, d represents the expected fraction of blank entries and will be referred to as *dilution* or *sparseness* (e.g., see [37–41]). Hence, with probability $1-d$ the example entry is non-zero, but still it can be affected by an error (i.e., $\xi_i^{\mu,A} \neq \xi_i^\mu$) with probability $\frac{1-r}{2}$. For this reason, r is named *quality* of the dataset [15, 19, 25]. With this definition, the two-entry correlation in each example is $\mathbb{E}[\xi_i^{\mu,A} \xi_j^{\mu,A}] = \delta_{ij}$, and, given two examples $\boldsymbol{\xi}^{\mu,A}$ and $\boldsymbol{\xi}^{\nu,B}$, they are independent if $\mu \neq \nu$ and correlated if $\mu = \nu$, due to the fact that they stem from the same the ground-truth $\boldsymbol{\xi}^\mu$. These remarks can be summarized by the following formulas

$$\mathbb{E}[\xi_i^{\mu,A}] = 0 \quad (2.5)$$

$$\mathbb{E}[(\xi_i^{\mu,A})^2] = (1-d) \quad (2.6)$$

$$\mathbb{E}[\xi_i^{\mu,A} \xi_j^{\nu,B}] = \delta_{i,j} (1-d)^2 [r^2 + \delta_{\mu,\nu} \delta_{A,B} (1-r^2)] \quad (2.7)$$

$$\mathbb{E}[\xi_i^{\mu,A} \xi_j^\nu] = \delta_{i,j} \delta_{\mu,\nu} (1-d)r, \quad (2.8)$$

where \mathbb{E} denotes the expectation with respect to the joint distribution $\mathcal{P}(\boldsymbol{\xi}, \boldsymbol{\chi}) = \mathcal{P}(\boldsymbol{\xi}) \mathcal{P}(\boldsymbol{\chi})$, see (2.2) and (2.4).

Given a sample of examples, there may be a teacher who classifies examples according to the corresponding archetype and we refer to this setting as **supervised**. Exploiting such information, we can determine class-wise means as

$$\bar{\boldsymbol{\xi}}^\mu := \frac{1}{M} \sum_{A=1}^M \boldsymbol{\xi}^{\mu,A} \in [-1, 1]^N$$

¹Since in this paper we only deal with ANNs within the Hebbian scheme, we choose to use the notation $\mathbf{\Gamma}$ for the coupling matrices to distinguish from a generic choice \mathbf{J} . Different prescriptions for the coupling matrix (leading to different ANN models) can be considered, possibly yielding to larger affordable loads, such as Kohonen's projection matrix [29] $\mathbf{X}(\mathbf{X}^T \mathbf{X})^{-1} \mathbf{X}^T$ which reaches the capacity upper bound $\alpha = 1$ [30] and the more general dreaming kernel $\mathbf{X}(\mathbf{I} + t)(\mathbf{I} + t \mathbf{X}^T \mathbf{X})^{-1} \mathbf{X}^T$, where $t \in \mathbb{R}^+$ is a tuneable parameter and which saturates to $\alpha = 1$ as $t \rightarrow \infty$ [22, 31–33].

and identify these as empirical representations of the ground-truth ξ^μ . Hence, in this case, we define the supervised Hebbian matrix as

$$\Gamma_{i,j}^s = \frac{1}{N} \sum_{\mu=1}^K \bar{\xi}_i^\mu \bar{\xi}_j^\mu, \quad \forall i, j \in \{1, \dots, N\}, \quad (2.9)$$

or, in matrix form, as $\mathbf{\Gamma}^s = N^{-1} \bar{\mathbf{X}} \bar{\mathbf{X}}^T$, where $\bar{\mathbf{X}}$ is a $N \times K$ matrix, storing all the means of the examples, thus $\bar{X}_{i,\mu} = \bar{\xi}_i^\mu$ for all $i \in \{1, \dots, N\}$ and $\mu \in \{1, \dots, K\}$.

In the end, we deal with the **unsupervised** setting, where classes remain disclosed and we cannot cluster examples. Thus, the least biased interaction matrix (see App. A and [22]) is given by the following unsupervised Hebbian matrix that reads as

$$\Gamma_{i,j}^u = \frac{1}{P} \sum_{\mu,A} \xi_i^{\mu,A} \xi_j^{\mu,A}, \quad \forall i, j \in \{1, \dots, N\}, \quad (2.10)$$

where $P = MN$, namely $\mathbf{\Gamma}^u = P^{-1} \mathbf{X}^{\text{ex}} \mathbf{X}^{\text{ex}T}$, where \mathbf{X}^{ex} is a $N \times KM$ matrix, storing all the single examples $X_{i,(\mu,A)}^{\text{ex}} = \xi_i^{\mu,A}$, for $i = 1, \dots, N$, $\mu = 1, \dots, K$, and $A = 1, \dots, M$.

Before concluding this section, we emphasize that the setting considered here is slightly different than that explored in [41], where ground-truth patterns themselves were affected by dilution and the noise in examples could preserve the arrangement of blank entries or possibly replace them with random binary entries. In that scenario, the dilution in ground-truth patterns was shown to give rise to “parallel learning”, namely the simultaneous learning of multiple patterns.

Further, it is worth specifying that the sparsity in the examples can be an intrinsic feature of the empirical realizations of the ground patterns, or it can derive from external operation, e.g., mimicking the dropout technique, as discussed in the App. A. In the former case, we expect that dilution affects both training and validation examples, while, in the latter, we expect that it acts on the level of training examples only, and thus it is only involved in the construction of the coupling matrix, while validation examples will only be characterized by the quality parameter r . In this paper, we will pursue the second picture.

3 Spectra of coupling matrices

In this Section, we compute the asymptotic spectral distribution of the coupling matrices $\mathbf{\Gamma}$, $\mathbf{\Gamma}^s$ and $\mathbf{\Gamma}^u$, introduced before. In particular, in the basic storing and supervised settings, we can directly apply the Marchenko-Pastur theorem, which is recalled in App. B, while in the unsupervised setting we will rely on some approximations. We start recalling the asymptotic spectral distribution for the basic storing Hebbian matrix [42].

Proposition 1. *Let $\mathbf{\Gamma}$ be the Hebbian matrix in the basic storing setting (2.3) and $\mu_{\mathbf{\Gamma}}$ the empirical distribution of its eigenvalues $\{\lambda_j^{\mathbf{\Gamma}}\}_{j=1,\dots,N}$, that is,*

$$\mu_{\mathbf{\Gamma}}(x) = \frac{1}{N} \#\{j \leq N : \lambda_j^{\mathbf{\Gamma}} < x\}. \quad (3.1)$$

Then, in the thermodynamic limit $N \rightarrow \infty$, $\mu_{\mathbf{\Gamma}}$ converges to a Marchenko-Pastur distribution $MP(\alpha, \alpha)$, with probability measure

$$d\mu(\lambda) = (1 - \alpha)\delta_{\lambda,0}d\lambda + \alpha d\mu_{\text{bulk}}(\lambda), \quad (3.2)$$

where

$$d\mu_{bulk}(\lambda) = \frac{1}{2\pi} \frac{\sqrt{(\lambda_+^0 - \lambda)(\lambda - \lambda_-^0)}}{\alpha\lambda} \mathbf{1}_{\lambda \in [\lambda_-^0, \lambda_+^0]} d\lambda, \quad (3.3)$$

and where $\lambda_{\pm}^0 = (1 \pm \sqrt{\alpha})^2$.

Let us now move to the supervised setting. This represents a relatively simple generalization of the basic storing setting, in fact, after noticing that

$$\mathbb{E}[\sqrt{\alpha}\bar{\xi}_i^\mu] = 0, \quad \mathbb{E}[(\sqrt{\alpha}\bar{\xi}_i^\mu)^2] = \alpha(1-d) \left((1-d)r^2 + \frac{1 - (1-d)r^2}{M} \right),$$

we can proceed as in Prop. 1, and state the following

Proposition 2. *Let Γ^s be the Hebbian matrix in the supervised setting (2.9) and μ_{Γ^s} the empirical distribution of its eigenvalues $\{\lambda_j^{\Gamma^s}\}_{j=1,\dots,N}$, that is*

$$\mu_{\Gamma^s}(x) = \frac{1}{N} \#\{j \leq N : \lambda_j^{\Gamma^s} < x\}. \quad (3.4)$$

Then, in the thermodynamic limit $N \rightarrow \infty$, μ_{Γ^s} converges to a Marchenko-Pastur distribution $MP(\alpha, \alpha\sigma^s(r, d, M))$, with probability measure

$$d\mu^s(\lambda) = (1-\alpha)\delta_{\lambda,0}d\lambda + \alpha d\mu_{bulk}^s(\lambda), \quad (3.5)$$

with

$$d\mu_{bulk}^s(\lambda) = \frac{1}{2\pi} \frac{\sqrt{(\lambda_+^s - \lambda)(\lambda - \lambda_-^s)}}{\alpha\sigma^s(r, d, M)\lambda} \mathbf{1}_{\lambda \in [\lambda_-^s, \lambda_+^s]} d\lambda, \quad (3.6)$$

$\lambda_{\pm}^s = \sigma^s(r, d, M) (1 \pm \sqrt{\alpha})^2$, and

$$\sigma^s(r, d, M) = (1-d) \left((1-d)r^2 + \frac{1 - (1-d)r^2}{M} \right). \quad (3.7)$$

Remark 1. *A convenient control parameter to assess the information content in the synthetic dataset is $\rho := \frac{1 - (1-d)r^2}{M(1-d)r^2}$. In fact, proceeding similarly to [15, 25], we find $\text{Prob}(\text{sgn}(\sum_a \chi_i^{\mu_a}) = -1) \approx 1 - \text{erf}(1/\sqrt{2\rho})$, for $M \gg 1$. Thus, the conditional entropy $H(\xi_i^\mu | \{\xi_i^{\mu_a}\}_A)$, which quantifies the amount of information needed to describe the original message ξ_i^μ , given the examples related to it, increases monotonically with ρ . Moreover, we can write $\sigma^s = (1-d)^2 r^2 (1 + \rho)$.*

Remark 2. *The result in Prop. 2 is an improvement compared to [42], as it takes into account the number of examples M without assuming $M \rightarrow \infty$.*

In the basic storing and in the supervised settings we are able to directly apply the Marchenko-Pastur theorem to compute the spectral distribution. This is possible as we can write the related coupling matrices of Wishart form². Moreover, looking at the definition in the unsupervised setting (2.10), we observe that the factors \mathbf{X}^{ex} have identically distributed but not independent entries, as the examples related to the same archetype are correlated. For this reason, in the unsupervised setting we introduce the Approximate Factorization Method (AFM), to compute *approximately* the spectral distribution of this coupling matrix and capture the crucial scalings between the relevant parameters, which we define as following

²A Wishart matrix is a random matrix of the form $\frac{1}{K} \mathbf{Y} \mathbf{Y}^T$, where \mathbf{Y} has i.i.d. entries. In this paper, we will often refer to matrices with Gram's form as Wishart-like matrices to stress their structure of covariance matrices, even though the entries are not independent

Definition 1 (Approximate Factorization Method). Let $\{z_{i,j}^\mu\}_{\mu,i,j}$ be a class of random variables, where each couple $z_{i,j}^\mu$ and $z_{k,l}^\nu$ are independent if $\mu \neq \nu$ or $i \neq k$, $i \neq l$, $j \neq k$ and $j \neq l$. Under the AFM we assume that there exists a class of i.i.d random variables $\{\phi_i^\mu\}_{\mu,i}$, such that

$$z_{i,j}^\mu \sim \phi_i^\mu \phi_j^\mu, \quad \forall \mu, \forall i \neq j. \quad (3.8)$$

A more detailed discussion about the validity and application of this approximation is provided in App. C.

Proposition 3. Let Γ^u be the Hebbian Matrix in the unsupervised setting (2.10) and μ_{Γ^u} the empirical distribution of its eigenvalues $\{\lambda_j^{\Gamma^u}\}_{j=1,\dots,N}$, that is,

$$\mu_{\Gamma^u}(x) = \frac{1}{N} \#\{j \leq N : \lambda_j^{\Gamma^u} < x\}. \quad (3.9)$$

By virtue of the AFM, in the thermodynamic limit $N \rightarrow \infty$, μ_{Γ^u} converges to a Marchenko-Pastur distribution $MP(\alpha, \alpha\sigma^u(r, d, M), \alpha(1-d-\sigma^u(r, d, M)))^3$, with probability measure

$$d\mu^u(\lambda) = (1-\alpha)\delta(\lambda - \alpha(1-d-\sigma^u(r, d, M)))d\lambda + \alpha d\mu_{bulk}^u(\lambda), \quad (3.10)$$

with

$$d\mu_{bulk}^u(\lambda) = \frac{1}{2\pi\alpha\sigma^u(r, d, M)[\lambda - \alpha(1-\sigma^u(r, d, M))]} \sqrt{(\lambda_+^u - \lambda)(\lambda - \lambda_-^u)} \mathbf{1}_{\lambda \in [\lambda_-^u, \lambda_+^u]} d\lambda, \quad (3.11)$$

$\lambda_\pm^u = \sigma^u(r, d, M)(1 \pm \sqrt{\alpha})^2 + \alpha(1 - \sigma^u(r, d, M))$ and

$$\sigma^u(r, d, M) = \sqrt{(1-d)^4 r^4 + (1-d)^2 \frac{1 - (1-d)^2 r^4}{M}}. \quad (3.12)$$

The proof of Props. 1 and 3 can be found, respectively, in Apps. B.1 and B.2, along with numerical checks to corroborate the validity of these results even at relatively small network and dataset sizes (i.e., $N \sim 10^2$, $M \sim 10$).

4 Validity of the models with examples: squared error

When dealing with examples of unavailable patterns, either in supervised or unsupervised settings, it is natural to question whether our empirical models account for a good representation of the reality, namely whether Γ^s and Γ^u are close to Γ , where we directly store the patterns. In this section, we use the Frobenius norm to estimate a squared distance between the empirical and the ideal coupling matrices, which is interpreted as *squared error* [43]. In addition, we discuss how the parameters α , r , d and M affect this error.

We start recalling the definition of the (normalized) Frobenius Norm $\|\cdot\|_F$ for a $N \times N$ real matrix \mathbf{A} (see also App. D for more details):

$$\|\mathbf{A}\|_F := \sqrt{\frac{1}{N} \sum_{i=1}^N \sum_{j=1}^N A_{i,j}^2} = \sqrt{\frac{1}{N} \sum_{i=1}^N \lambda_i^2} \xrightarrow{N \rightarrow \infty} \sqrt{\mathbb{E}[\lambda_{\mathbf{A}}^2]}, \quad (4.1)$$

where λ_i , $i = 1, \dots, N$ are the N eigenvalues of \mathbf{A} , and where with $\lambda_{\mathbf{A}}$ we denote a stochastic variable distributed according to the asymptotic empirical distribution of the eigenvalues of \mathbf{A} . This suggests a mathematically sound definition of squared error for random matrices:

³Here we are introducing an unconventional notation, by adding a third argument for the Marchenko-Pastur distribution to specify the shift in the distribution.

Definition 2. Let \mathbf{A} and \mathbf{B} be two $N \times N$ symmetric real random matrices. The Squared Error (SE) of \mathbf{B} w.r.t. \mathbf{A} is defined as:

$$\mathcal{E}(\mathbf{A}, \mathbf{B}) = \|\mathbf{A} - \mathbf{B}\|_F^2. \quad (4.2)$$

Thus, in order to compute $\mathcal{E}(\mathbf{\Gamma}^{s,u}, \mathbf{\Gamma})$ in the thermodynamic limit $N \rightarrow \infty$, we will have to compute the limit of the second non-centered moment of the empirical spectral distribution of $\mathbf{\Gamma}^{s,u} - \mathbf{\Gamma}$, which we will be able to do by leveraging the results collected in Sec. 3 and by applying the AFM.⁴ Hereafter we directly report our results, collecting the technicalities in App. D.

For the supervised case, we find

$$\mathcal{E}(\mathbf{\Gamma}^s, \mathbf{\Gamma}) = \|\mathbf{\Gamma}^s - \mathbf{\Gamma}\|_F^2 = \quad (4.3)$$

$$= \alpha[1 - 2(1-d)^2 r^2 + (\sigma^s)^2 + 2\alpha(\sigma^s - 1)^2] = \quad (4.4)$$

$$= \alpha[1 - 2(1-d)^2 r^2 + (1-d)^4 r^4 (1+\rho)^2 + 2\alpha((1-d)^2 r^2 (1+\rho) - 1)^2], \quad (4.5)$$

where σ^s is defined in Eq. (3.7). Likewise, in the unsupervised case we find

$$\mathcal{E}(\mathbf{\Gamma}^u, \mathbf{\Gamma}) = \|\mathbf{\Gamma}^u - \mathbf{\Gamma}\|_F^2 = \quad (4.6)$$

$$= \alpha[(1 - (1-d)^2 r^2)^2 + (1-d)^2 \frac{1 - (1-d)^2 r^4}{M} + \alpha d^2] = \quad (4.7)$$

$$= \alpha[1 - 2(1-d)^2 r^2 + (\sigma^u)^2 + \alpha d^2], \quad (4.8)$$

where σ^u is defined in Eq. (3.12). These analytical results highlight that $\mathcal{E}(\mathbf{\Gamma}^s, \mathbf{\Gamma})$ and $\mathcal{E}(\mathbf{\Gamma}^u, \mathbf{\Gamma})$ decrease in r, M and increase in d . The dependence on M and r is intuitive, because as M or r grow, the data set $\{\xi^{\mu,A}\}_{\mu=1,\dots,K}^{A=1,\dots,M}$ becomes more and more informative on the archetypes $\{\xi^\mu\}_{\mu=1,\dots,K}$, so that $\mathbf{\Gamma}^{s,u}$ provides a better approximation of $\mathbf{\Gamma}$. However, the larger d , the more insensitive the SE becomes to the quality of the examples r . Moreover, we can state that both SEs grow with α , the dependence being quadratic (but in the unsupervised case the dependence becomes linear when $d = 0$). The numerical simulations shown in Fig. 2 (upper and lower panels, respectively) confirm these remarks and corroborate the AFM in the evaluation of the SE, as the analytical estimates accurately fit the empirical data (even for relatively small sizes, $N \sim 10^2$ and $M \sim 10$).

5 1-step stability, attractiveness and capacity of generalization

In this section, we inspect the generalization capabilities of a neural network endowed with the supervised and unsupervised Hebbian interaction matrix. In the first part, we will introduce some useful and general definitions for the stability and the attractiveness of arbitrary configurations (including, for instance, mixtures, see [44]), next, we will compute the stability and attractiveness for the patterns ξ^μ and the stability for the examples.

Let us consider a certain target configuration \mathbf{x} and another configuration \mathbf{x}' , lying on the boundary of the Hamming ball $\mathcal{B}_R(\mathbf{x})$ centered in \mathbf{x} and with (normalized) radius R . These boundaries can be realized by perturbing \mathbf{x} as $\mathbf{x} \rightarrow \mathbf{x}' = \boldsymbol{\eta} \odot \mathbf{x}$, with $\eta_i \underset{i.i.d.}{\sim} \text{Rad}(p)$, $\forall i \in \{1, \dots, N\}$ and independent of the coupling matrix \mathbf{J} and the initial configuration \mathbf{x} . Indeed, choosing $p = 1 - 2R$,

$$d_H(\mathbf{x}', \mathbf{x}) = \frac{1}{2N} \sum_i (1 - \eta_i) \underset{N \gg 1}{\approx} \frac{1}{2} (1 - p) = R.$$

⁴Here this is necessary also in the supervised case because of the product $\mathbf{\Gamma}\mathbf{\Gamma}^s$ resulting from the square $(\mathbf{\Gamma}^s - \mathbf{\Gamma})^2$.

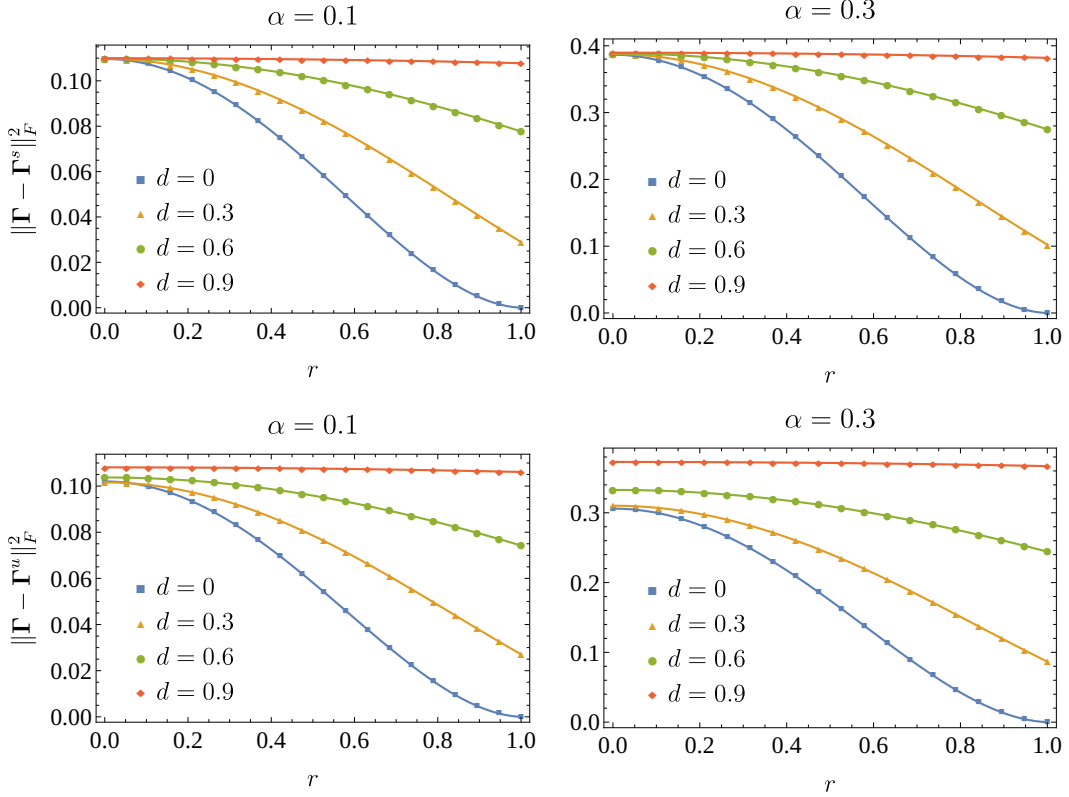


Figure 2. Comparison of the squared error between basic storing and supervised (upper panels) or unsupervised (lower panels) settings. The plots compare numerical results (dots) and theoretical predictions (4.4) and (4.8) (solid curves) for the (normalized) Frobenius norm between Γ and, respectively, Γ^s and Γ^u for $\alpha = 0.1$ (left) and $\alpha = 0.3$ (right) for fixed $M = 50$ and different choices for d , as a function of the dataset quality r . Numerical results are averaged over 30 different realizations of the coupling matrices. The network size is $N = 1000$. Error bars are not reported, as the relative error is very low.

Then, we can take \mathbf{x}' as initial configuration $\boldsymbol{\sigma}^{(0)} = \mathbf{x}'$ and apply (2.1) to get $\boldsymbol{\sigma}^{(1)}$. Next, multiplying both sides of the evolution relation by x_i , we obtain

$$\sigma_i^{(1)} x_i = \text{sgn}\left(\sum_{j=1}^N J_{i,j} x_j \eta_j x_i\right).$$

A positive argument of the sign function means that, in a single step, the state of the i -th neuron has remained (or has flipped to get) equal to the target x_i . This motivates the following

Definition 3. Given two configurations \mathbf{x} and $\mathbf{x}' = \boldsymbol{\eta} \odot \mathbf{x}$, with $\eta_i \underset{i.i.d.}{\sim} \text{Rad}(p)$, the attractiveness of the i -th neuron in \mathbf{x} w.r.t. \mathbf{x}' is the random variable

$$\Delta_i(\mathbf{x}, \boldsymbol{\eta}) = \sum_{j=1}^N J_{i,j} x_j \eta_j x_i. \quad (5.1)$$

When $p = 1$, that is, when the initial state coincides with \mathbf{x} , $\Delta_i(\mathbf{x}, \boldsymbol{\eta})$ tells us whether the state of the neuron i is invariant ($\Delta_i(\mathbf{x}) = 1$) or not ($\Delta_i(\mathbf{x}) = -1$). Recalling that \mathbf{x}' is taken as the

initial configuration and \mathbf{x} is a target configuration, we can restate these concepts by introducing the configuration overlaps

$$m^{(0)}(\mathbf{x}, \boldsymbol{\eta}) = \frac{1}{N} \sum_{i=1}^N x_i \sigma_i^{(0)} = \frac{1}{N} \sum_{i=1}^N \eta_i, \quad (5.2)$$

$$m^{(1)}(\mathbf{x}, \boldsymbol{\eta}) = \frac{1}{N} \sum_{i=1}^N x_i \sigma_i^{(1)} = \frac{1}{N} \sum_{i=1}^N \text{sgn}[\Delta_i(\mathbf{x}, \boldsymbol{\eta})], \quad (5.3)$$

and say that \mathbf{x} is attracting $\boldsymbol{\sigma}^{(0)}$ if $m^{(1)} > m^{(0)}$. When \mathbf{x} coincides with a pattern, the overlaps above are also known as Mattis magnetizations (related to that pattern) evaluated at time steps $n = 0, 1$.

In order to further simplify the computations and obtain closed-form expressions for the 1-step Mattis magnetization, we will carry out our computations under the definition below

Definition 4 (Gaussian approximation). *Within the Gaussian approximation (GA), we assume that the attractivenesses Δ_i are i.i.d. Gaussian random variables, i.e. $\Delta_i \sim_{i.i.d.} \mathcal{N}(\mu_1, \mu_2 - \mu_1^2)$. A discussion on the validity of this approximation is provided in [42].*

Remark 3. *The quantities μ_1 and μ_2 in the previous definition clearly stands for the first two non-centered moments of the distribution of the attractiveness Δ_i . A crucial point is that, within the GA and in the thermodynamic limit, these two moments can be analytically estimated and turn out to be functions of the model parameters (that is, α , M , r and d) and of the probability p only.*

Within the GA and in the thermodynamic limit, the 1-step overlap w.r.t. the reference configuration \mathbf{x} does not depend on $\boldsymbol{\eta}$ but directly on the parameter p ; then we can define it as

$$m^{(1)}(\mathbf{x}, p) := \lim_{N \rightarrow \infty} m^{(1)}(\mathbf{x}, \boldsymbol{\eta}). \quad (5.4)$$

Using again the GA and in the thermodynamic limit, we have

$$m^{(1)}(\mathbf{x}, p) = \lim_{N \rightarrow \infty} \frac{1}{N} \sum_{i=1}^N \text{sgn}[\Delta_i(\mathbf{x}, \boldsymbol{\eta})] = 2\mathcal{P}(\Delta_i \geq 0) - 1 = \text{erf}\left(\frac{\mu_1}{\sqrt{2(\mu_2 - \mu_1^2)}}\right). \quad (5.5)$$

In the following proposition, we finally express the moments $\mu_{1,2}$ in terms of finite moments of a generic Marchenko-Pastur law.

Remark 4. *This approach is closely related to the signal-to-noise technique [45]. In fact, requiring $m^{(1)}(\mathbf{x}, \boldsymbol{\eta})$ to be larger than a certain threshold, specifically $m^{(1)}(\mathbf{x}, \boldsymbol{\eta}) > \text{sign}(\frac{1}{\sqrt{2}}) \approx 0.68$, we get $\mu_1 > |(\mu_2 - \mu_1^2)|$. In terms of the quantities Δ_i , this is nothing but the requirement that $\mathbb{E}(\Delta_i) / \sqrt{\text{Var}(\Delta_i)} > 1$, with the numerator and denominator in the last inequality interpreted as, respectively, signal and noise. We will deepen this point in App. E.*

Proposition 4. *In the thermodynamic limit and under the GA, the first and second moments of the attractiveness of the concepts $\boldsymbol{\xi}^\mu$ in the supervised and unsupervised cases read*

$$\mu_1^{s/u} = \frac{p}{2\alpha} (\kappa^2(\alpha, \sigma^{s/u}, s^{s/u}) + \kappa^2(\alpha, 1, 0) - \kappa^2(\alpha, \sigma_\pm^{s/u}, s_\pm^{s/u})), \quad (5.6)$$

$$\begin{aligned} \mu_2^{s/u} &= (1 - p^2) \kappa^2(\alpha, \sigma^{s/u}, s^{s/u}) \\ &+ \frac{p^2}{6\alpha} (\kappa^3(\alpha, \sigma_+^{s/u}, s_+^{s/u}) + \kappa^3(\alpha, \sigma_-^{s/u}, s_-^{s/u}) - 3\kappa^3(\alpha, 1, 0)), \end{aligned} \quad (5.7)$$

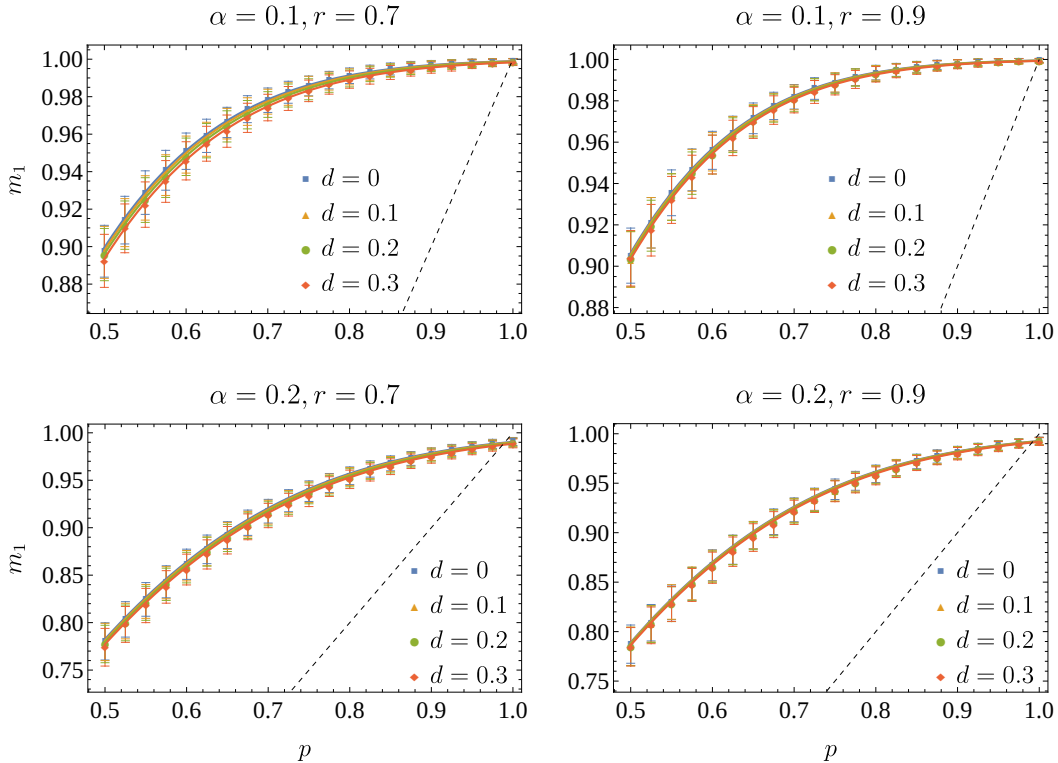


Figure 3. Attractiveness of archetypes in the supervised setting. The plots compare the theoretical (solid curves, drawn following Prop. 4) and the numerical estimates (dots) of $m^{(1)}(\xi, p)$ for the supervised setting. Numerical results are averaged over 100 different realizations with $N = 500, M = 100$ and various values of the dilution parameter: $d = 0, 0.1, 0.2, 0.3$. The first row refers to $\alpha = 0.1$ (for comparison, the critical storage capacity for the Hopfield model at zero-temperature is $\alpha_c = 0.138$), while in the second row $\alpha = 0.2$. The columns instead refers to different quality levels of the datasets employed in the construction of the coupling matrix: moderate quality ($r = 0.7$, left column), high-quality dataset ($r = 0.9$, right column).

where $\kappa^n(\sigma, \alpha, s)$ is the n -th moment of a MP (σ, α, s) , $\sigma_{\pm}^{s/u}$ and $s_{\pm}^{s/u}$ are defined as in Sec. 3,5 and $\sigma_{\pm}^{s/u}$ and $s_{\pm}^{s/u}$ are specified in the proof.

The proof of the Proposition is detailed in App. B.3. Since the explicit expressions are rather lengthy, here we simply report the plots of the theoretical predictions for the 1-step magnetization $m^{(1)}(\xi^{\mu}, p)$ based on Prop. 4, with a comparison with experimental findings, see Figs. 3 and 4 for the supervised and the unsupervised settings, respectively. In particular, for the former, our analytical estimates work accurately and, as expected, d does not influence much the result. Conversely, in the unsupervised setting, we found that the theoretical prediction as given by Prop. 4 tends to underestimate the role of the dilution in the 1-step Mattis magnetization. Specifically, the former show the same qualitative behavior of the numerical results as a function of the dilution parameter but differ quantitatively. Nevertheless, we can fit the numerical results using the same functional form

⁵We recall that the asymptotic distribution is derived by means of the AFM for the unsupervised setting. In addition, we set $s^s = 0$ to avoid redundancies in the statement of the proposition. Finally, notice that $\mu_i^{s/u}$ do not depend on the specific concept ξ^{μ} , because of the symmetry induced by Eq.2.2.

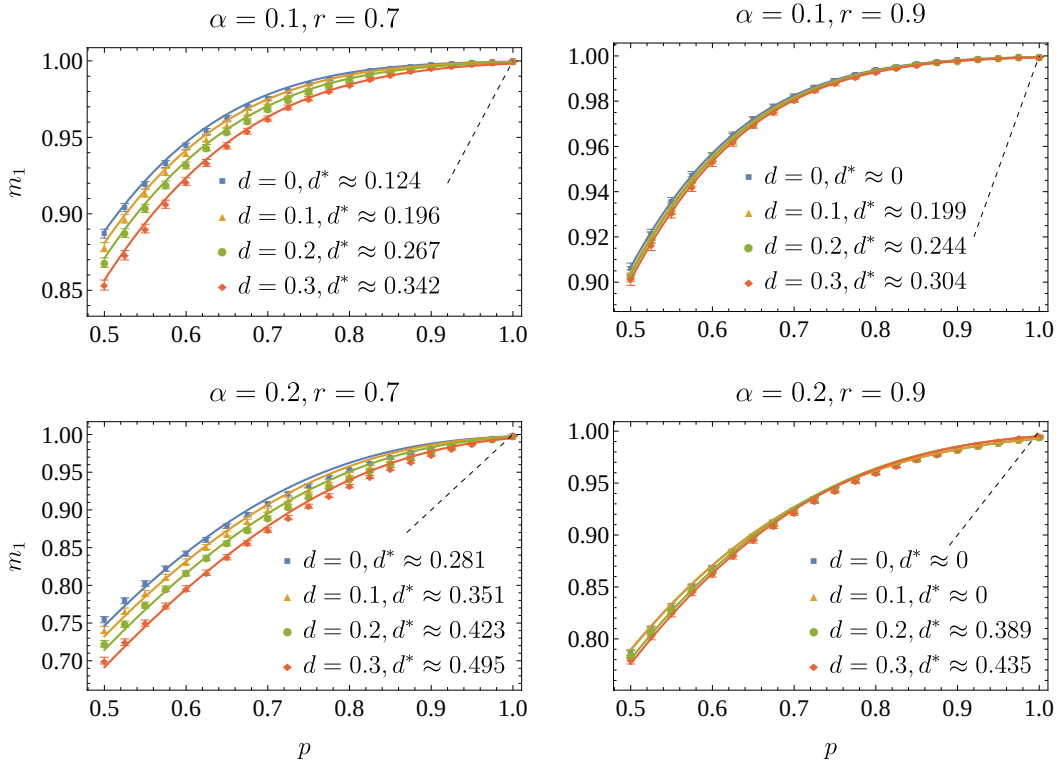


Figure 4. Attractiveness of archetypes in the unsupervised settings. The plots report a comparison between the numerical estimates (dots) at a dilution level d for the quantity $m^{(1)}(\xi, p)$ and the theoretical expressions for the best-fitting value d^* of the dilution – obtained comparing the predictions in Prop. 4 and the numerical findings – in the unsupervised setting. Numerical results are averaged over 100 for $N = 500$, $M = 100$ and $d = 0, 0.1, 0.2, 0.3$. The first and second rows refer resp. to $\alpha = 0.1$ and $\alpha = 0.2$, while left and right column refer resp. to moderate quality ($r = 0.7$) and almost perfect ($r = 0.9$) datasets. The coefficient of determination is $R^2 \approx 1$.

in terms of d , thus determining the best-fit parameter $d^*(\alpha, M, N, r)$.

Now, setting $p = r$ in Eqs. (5.5-5.7), we investigate the capacity of generalization of the network, namely the ability of the Hopfield model to reconstruct the ground pattern ξ^μ starting from a test example $\sigma^{(0)} = \xi^\mu \odot \tilde{\chi}$, with $\tilde{\chi}_i \sim \text{Rad}(r)$, distributed as a training example *without* dilution. Again, we find substantial agreement of the theoretical predictions and the numerical data in the supervised setting, with the dilution having mild (but negative) effects on the generalization capabilities of the model, as reported in Fig. 5. As for the unsupervised setting, the theoretical predictions again exhibit a general underestimation of the effects of dilution, hence, also in this case, we fit the analytical formulas with the numerical data and find a best-fitting value d^* , as reported in Fig. 6. Remarkably, our findings suggest that diluting the training dataset at high load α can yield a positive effect, as highlighted in the inset in Fig. 6, right plot.

In order to check that such behavior for the generalization capabilities is captured by the theoretical predictions, we analyze the evolution of the theoretical 1-step magnetization $m^{(1)}$ (exploiting Eq. (5.5) and Prop. 4) as a function of d , see Fig. 7. In the upper left plot ($\alpha = 0.1$), the magnetization is a non-increasing function of d regardless of the dataset quality r (while only results for high quality are

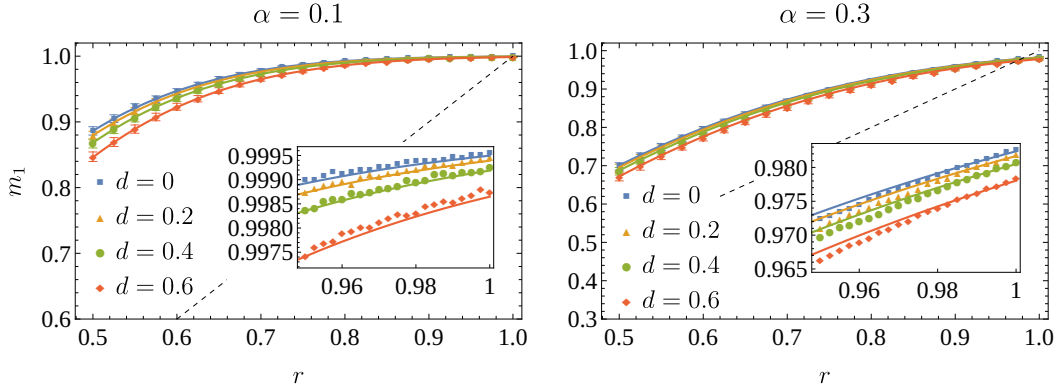


Figure 5. Generalization in the supervised setting. The plots show a comparison between the theoretical predictions (solid curves, as prescribed by Prop. 4 after setting $p = r$) and the numerical estimates (dots) of $m^{(1)}(\xi, r)$ for the supervised setting. Numerical results are averaged over 100 different realizations fixing $N = 500, M = 100$. We compare results for $\alpha = 0.1$ (left) and $\alpha = 0.3$ (right). The insets provide a zoom on the high-quality range to check the persistency of the trend with respect to d . Error bars are not reported, due to the low magnitude of the relative errors of the numerical simulations.

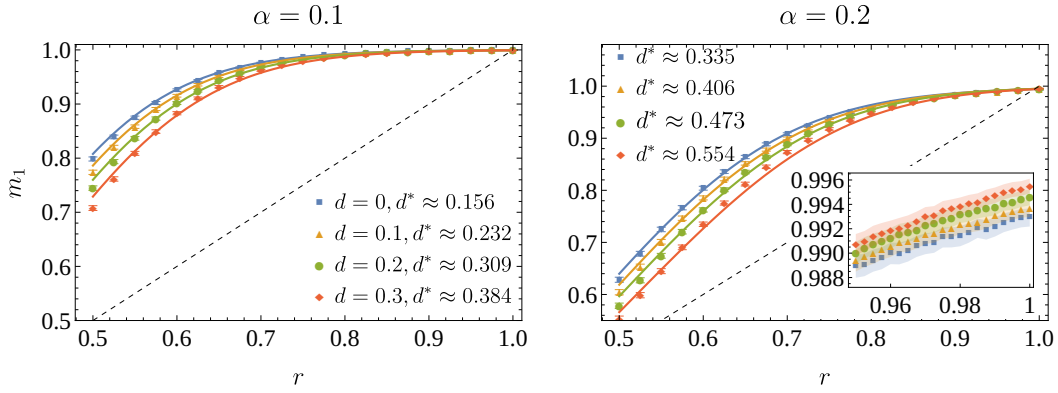


Figure 6. Generalization in the unsupervised setting. The plots show a comparison between the numerical estimates (dots) for the quantity $m^{(1)}(\xi, r)$ at a dilution level d and the theoretical expressions (solid curves) for the best-fitting value d^* – obtained comparing the predictions in Prop. 4 and the numerical findings – in the unsupervised setting. For the sake of readability, in the right plot we reported only the best-fitting ($R^2 \approx 1$) values d^* of the dilution parameters, which always refer (from top to bottom) to $d = 0, 0.1, 0.2, 0.3$ in the numerical simulations. Numerical results are averaged over 100 different realizations fixing $N = 500, M = 100$. We compare results for $\alpha = 0.1$ (left) and $\alpha = 0.2$ (right). For the latter, we also report a zoom on high values of the dataset quality ($r \simeq 1$, inset plot). Again, error bars are not reported, due to the low magnitude of the relative errors of the numerical simulations.

reported, the same situation holds for lower quality). Indeed, for a load below the Hopfield model’s critical storage capacity ($\alpha_c \approx 0.14$), the unsupervised setting is expected to effectively reconstruct the ground-truths without diluting the dataset, hence no beneficial effects are observed. On the other hand, increasing α , some non-trivial effects may emerge, depending on the interplay between dilution and the noise due to pattern interference, as we show hereafter. In the upper right plot ($\alpha = 0.4$),

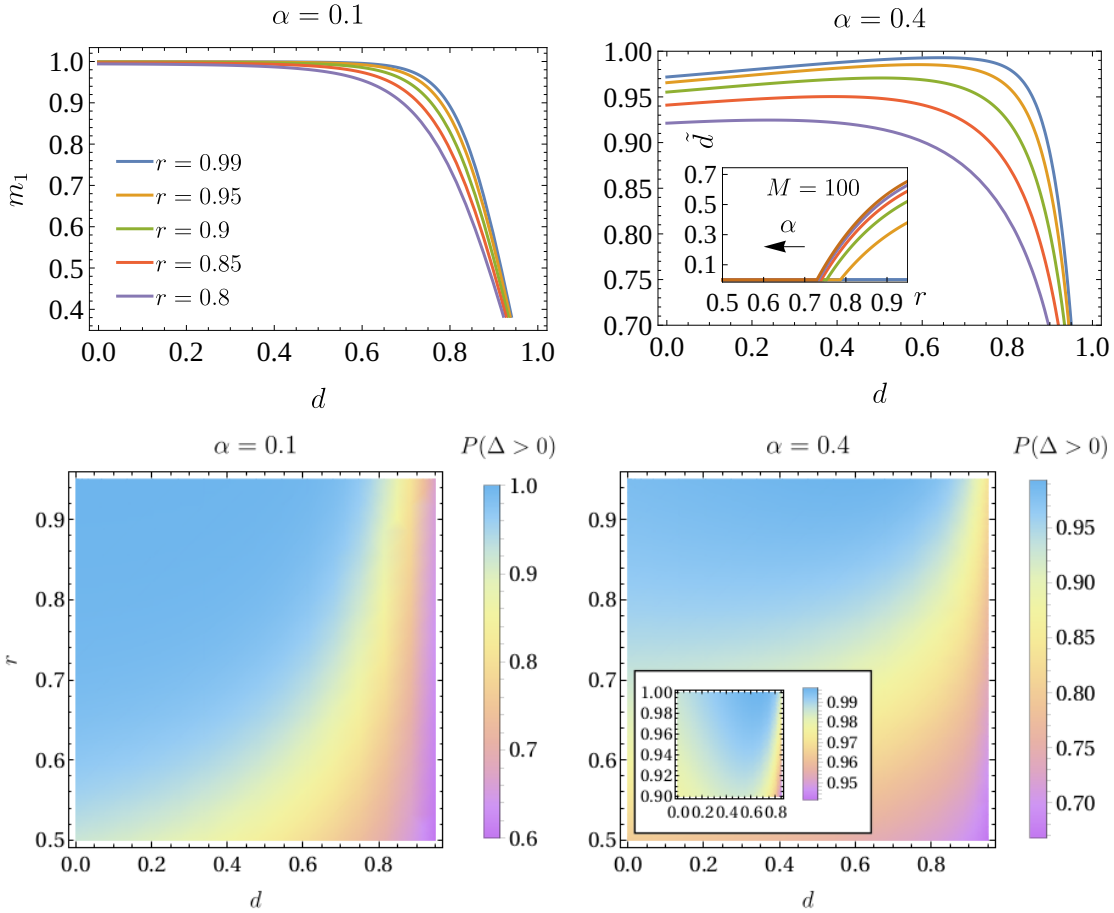


Figure 7. A resuming picture of the capacity of generalization in unsupervised setting. In the first row, we report the behavior of the 1-step Mattis magnetization as a function of the dilution parameter d for various values of r and $\alpha = 0.1$ (left) and $\alpha = 0.4$ (right). The inset in the upper right plot highlights the behavior of \tilde{d} (i.e., the values of the dilution parameter at which, for given r , the 1-step magnetization develops a maximum) as a function of the dataset quality, for different values of the load α (going from right side to the left side, $\alpha = 0.1, 0.2, 0.3, 0.4, 0.5, 0.6$). In the second row, we report the heat maps for the probability that the attractiveness of the ground-truth is positive, namely $\mathcal{P}(\Delta \geq 0) = \frac{1}{2}(1 + m^{(1)})$ – see also App. E, again for $\alpha = 0.1$ (left) and $\alpha = 0.4$. In the lower right plot, the inset reports a zoom to the portion of parameters plane $(r, d) \in (0.9 \div 1, 0 \div 1)$ for highlighting the non-monotonous behavior of the 1-step magnetization as a function of d . In all the plots, the number of examples per class is fixed to $M = 100$.

for high values of the quality, the 1-step magnetization turns out to be a non-monotonous function of d , and, in particular, it exhibits a maximum at some non-zero value of the dilution parameter (say \tilde{d}), with reconstruction capabilities progressively lost at higher d . In the inset of the same plot, we report the dependence of \tilde{d} on r for $M = 100$ and for various values of the load α . As we reasonably expect, the higher the load, the lower the threshold in r at which dilution is effective⁶. In the lower plots of Fig. 7, we report the color maps for the probability $\mathcal{P}(\Delta \geq 0)$, which – under the GA

⁶Recall that, at low α dilution is not needed, or it can be harmful on the generalization capabilities.

(Def. 4) and in the thermodynamic limit – is exactly $\frac{1}{2}(1 + m^{(1)})$, see also App. E. In the figure, we explore the plane (d, r) for all possible values of the dilution parameter and for reasonable high dataset quality. Again, at low load ($\alpha = 0.1$, lower left plot) and r high enough, dilution has no effects on the generalization capabilities of the model; conversely, high d results in a reduction of the probability $\mathcal{P}(\Delta \geq 0)$, leading to a breakdown of reconstruction capabilities. As for the high α case ($\alpha = 0.4$, lower right plot), dilution is beneficial for sufficiently high r , as can be also seen by inspecting the zoom reported in the inset: sparsing the training dataset here increases the probability of $\Delta \geq 0$, yielding better generalization capabilities w.r.t. non-diluted case.

So far, we used random matrix theory tools to outline a qualitative picture for the effects of dataset dilution strategies on the training dataset, both in the supervised and unsupervised settings. We emphasize that, in developing the theoretical framework for the latter scenario, we *i*) derived the spectral distribution by means of the AFM (1); *ii*) estimated analytically the generalization capabilities from 1-step dynamics under the GA (4) and in the thermodynamic limit. Even though the qualitative validity of our theoretical framework is evident, a quantitative check based on long-run Monte Carlo simulations is in order and will be addressed in the next section.

6 Numerical simulations for the unsupervised setting

In this section, we deepen the role of the dilution in the unsupervised setting by performing extensive numerical simulations where the system is let relax towards a fixed point following the dynamics (2.1). We will focus on the stability and the attractiveness of the ground-truths, and on the ability of the model to generalize from unseen data in a reconstruction task. In doing this, the dilution will only be inserted in the training data (that is, the examples from which we construct the coupling matrix \mathbf{J}): such a procedure can be interpreted as a dropout-like technique (traditionally used to avoid overfitting, see [8]) which is implemented by making “silent” a fraction d of the bits in the examples. This means that, when analyzing the generalization capabilities of the model, validation data are *not* diluted.

The numerical experiments are performed in this way. Depending on the feature under consideration (stability, attractiveness and generalization), we extract an initial condition $\sigma^{(0)}$ associated to a given pattern ξ^μ for some $\mu = 1, \dots, K$, and perform the Glauber dynamics (2.1) until the stability criterion $h_i^{(n)} \sigma_i^{(n)} > 0$ for all $i = 1, \dots, N$ is met, where $h_i^{(n)} = \sum_j J_{ij} \sigma_j^{(n)}$ is the local internal field acting on the i -th spin. The related configuration is therefore a fixed point, denoted as $\sigma^{(\infty)}$. Then, we compute the Mattis magnetization $m_f := m_\mu^{(\infty)} = \frac{1}{N} \sum_{i=1}^N \xi_i^\mu \sigma_i^{(\infty)}$. As for the initial conditions $\sigma^{(0)}$, we have:

- **Stability analysis:** in this case, the initial condition $\sigma^{(0)}$ is perfectly aligned with the pattern ξ^μ . For each realization of the training set $\{\xi^{\mu,A}\}$ (with corresponding patterns ξ^μ), we perform the stability analysis for each of the K ground-truth ξ^μ , and in the end average over 50 different realizations of the training set. The results, reported in Fig. 8, show the dependence on d of the magnetization m_f for various values of K ($= 50, 200, 250$), M ($= 10, 20, 200$) and r ($= 0.8, 0.9$);
- **Attractiveness analysis:** the initial condition $\sigma^{(0)}$ is a configuration consisting in randomly spin-flipping a fraction q of the bits in the patterns ξ^μ . The number of different initial conditions for each pattern is 500, then we perform the same analysis for all of the K ground-truths. The results, reported in Fig. 9, show the magnetization m_f as a function of $m_0 = \frac{1}{N} \sum_{i=1}^N \xi_i^\mu \sigma_i^{(0)}$ (which is a function of q) for different values of K ($= 50, 200, 500$), M ($= 10, 50, 200$), d ($= 0, 0.5$) and fixed $r = 0.95$;

- **Generalization analysis:** in this setup, the initial condition is a validation example, that is, a configuration $\tilde{\xi} = \tilde{\chi} \odot \xi^\mu$ with $P(\tilde{\chi}_i = \pm 1) = \frac{1 \pm r}{2}$. The number of different validation examples for each pattern is 500, then we perform the same analysis for all of the K ground-truths. The results, reported in Fig. 10, show the final magnetization m_f as a function of $m_0 = \frac{1}{N} \sum_{i=1}^N \tilde{\xi}_i \xi_i^\mu$ (which is a function of r) for different values of K ($= 50, 200, 250$), M ($= 10, 50, 200$) and d ($= 0, 0.5$).

Let us start with the pattern stability, whose results are organized in Fig. 8 as follows: the columns refer to different values of the number of classes in the training set ($K = 50, 250, 500$, corresponding to $\alpha = 0.05, 0.25, 0.5$), while the rows refer to different values of the dataset quality ($r = 0.6, 0.8, 0.9$). Each plot reports the results for $M = 10, 20, 200$. By inspecting the plots, we see that, at low load ($\alpha = 0.05$) the effect of the dilution is harmful at relatively low number of training points ($M = 10, 20$), as the final magnetization decays with d , but does not affect the stability of the patterns in presence of large redundancy in the dataset ($M = 200$). The situation is robust w.r.t. the quality parameter r , with the only quantitative differences in the final magnetization m_f . Increasing the load at $\alpha = 0.25$ (above the Hopfield model critical threshold), the situation slightly changes, as – especially for high-quality large enough training datasets – the stability of the ground-truths is enhanced by supplying the network with high enough (that is, $d \gtrsim 0.4$) diluted examples. Take for instance the case $M = 200$: increasing the quality from $r = 0.6$ (where ground-truths are always fixed point for the neural dynamics) to $r = 0.9$, we see that the stability of the hidden patterns decreases (in average) for non-diluted training samples; in this case, introducing dilution is crucial to regain stability of the ground-truths. This is more evident by further increasing the load α (that is, $K = 500$, right column): dealing with high-quality examples would require both large M and dilution d in order to ensure stability of the hidden patterns. Thus, these findings corroborate our expectations about the positive role of dilution at high α (and high M), as suggested by the theory.

We now move our attention to the attracting capabilities of hidden patterns: the related results are reported in Fig. 9 and are organized as follows. In all of the simulations, the quality of the dataset is fixed $r = 0.95$ (dilution is beneficial for high-quality datasets, as also highlighted in the afore discussed results about patterns stability). The left, middle and right columns refer to low ($M = 10$), intermediate ($M = 50$) and high ($M = 200$) examples per class, while the rows refer to $K = 50$, $K = 200$ and $K = 500$ (corresponding to $\alpha = 0.05, 0.2, 0.5$). Each plot displays the results for $d = 0$ (blue points) and $d = 0.5$ (yellow points). The dashed curve represents $m_0 = m_f$: if the experimental data are above the curve, the dynamics results in configuration closer to the ground truths. For $K = 50$ (first row), dilution has (harmful but slight) effects only for low number of examples M , while for large datasets (with fixed K) both for the diluted and non-diluted Hopfield models archetypes are strongly attractive. A similar situation takes place just above the critical threshold of the Hopfield model (that is, $K = 200$ corresponding to $K/N = 0.2 \gtrsim 0.14$). The crucial difference lies in the fact that the magnetization m_f depends non-trivially on the initial condition, even though the ground truths still exhibit a relevant attractive power, with the diluted model slightly performing better than the usual Hopfield model at very large dataset ($M = 200$). We emphasize that, in such a situation, the true attractors seem not to be precisely located at the hidden patterns (as $m_f = m_0(q)$ for values of q less than 1), but on balls centered around them with a relatively small radius. This situation is well-known in the context of Hopfield model in the oversaturated regime, see for example [46]. Finally, far above the critical threshold $\alpha_c = 0.14$ (that is, for $K = 500$) the diluted model always performs better w.r.t. the usual Hopfield network, and increasing the dataset size (e.g. $M = 200$) allows the former to have

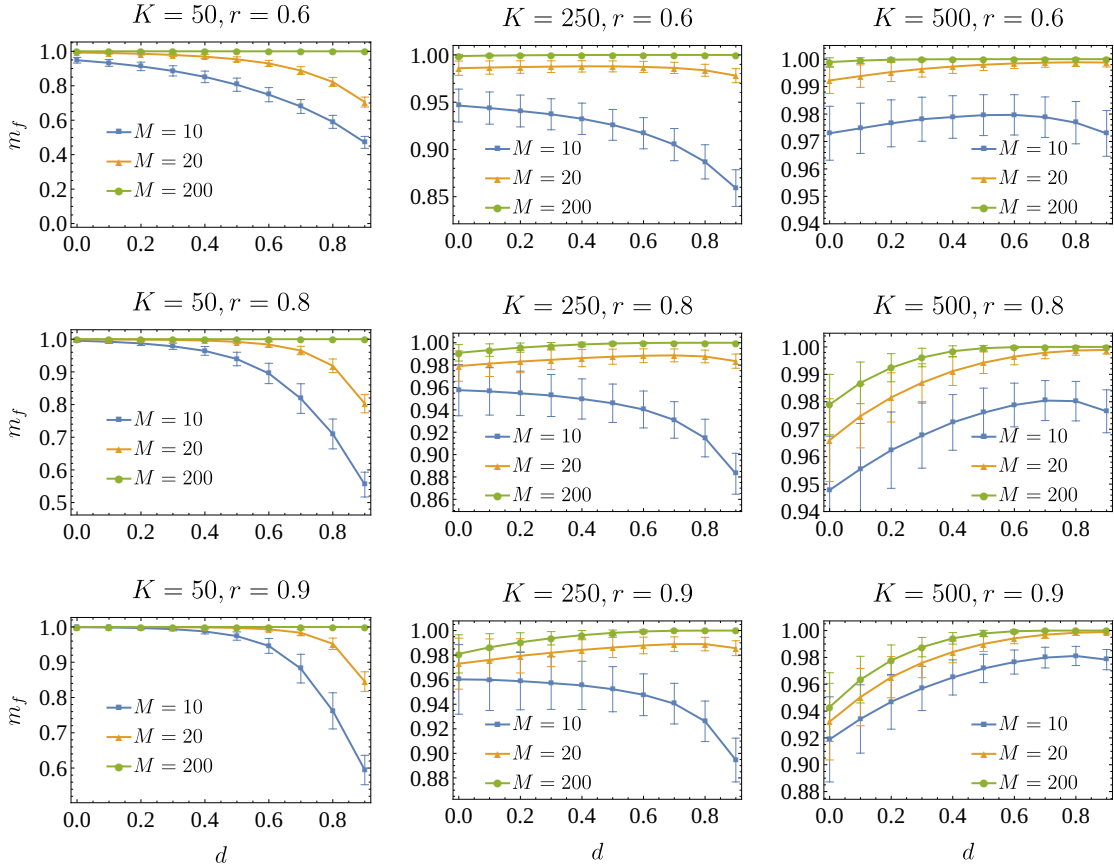


Figure 8. Pattern stability as a function of the dilution in the unsupervised setting. The plots report the behavior of the final magnetization m_f of the neural dynamics (2.1) with the initial condition being the one of the ground-truth ($\sigma^{(0)} = \xi^\mu$). We report the dependence of m_f on the dilution parameter d for various values of K (50, left; 250, center; 500, right), the dataset quality r (0.6, first row; 0.8, second row; 0.9, third row), and the number of examples per class M (10, blue square dots; 20, yellow triangles; 200, green circles). The network size is fixed to $N = 1000$. The results are averaged over 500 different realizations of the couplings matrix for each point.

a final magnetization higher than the one relative to the starting condition ($m_f > m_0$). However, the attracting power of hidden patterns is very limited in this situation.

Finally, we consider the effects of dilution on the generalization capabilities of these networks. As we said above, the starting configuration is an example with the same quality of the training dataset, but *without* the dilution, as the latter is inserted by hand in the construction of the coupling matrix. We perform experiments analogous to the preceding ones, but, now, the initial magnetization m_0 is a function of r , and the quality of the training dataset varies accordingly. At low K , the situation is similar to the previous analysis: for low number of examples, the non-diluted network exhibits better generalization performances, and the two models have comparable pattern reconstruction capabilities in the large dataset case (in particular, the generalization performances are high, as $m_f \sim 1$ for $M = 200$ both for $d = 0$ and $d = 0.5$). Turning to relatively large loads, a large M and high dilution

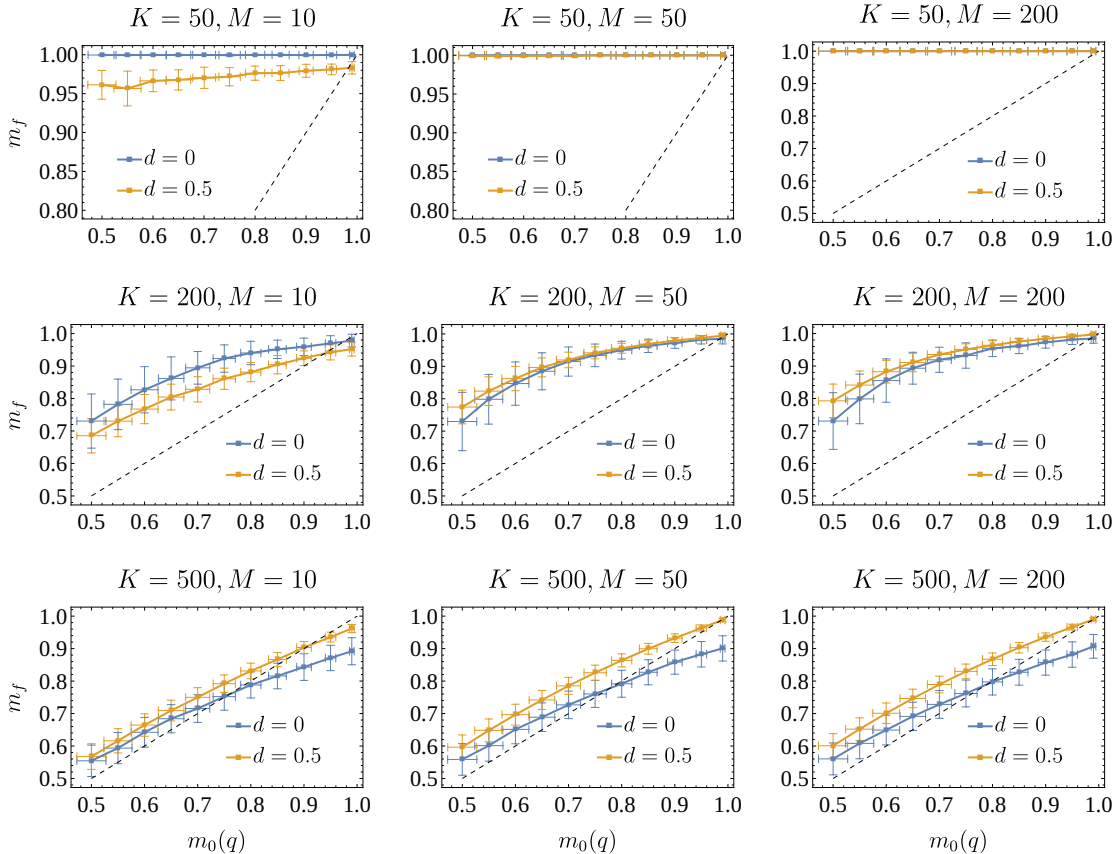


Figure 9. Pattern attractiveness in the unsupervised setting. The plots report the results of the pattern attractiveness, namely the final magnetization m_f under the relaxation to fixed points of the neural dynamics (2.1) starting from a perturbed version of the ground-truth with a fraction q of random spin flips (with initial magnetization $m_0(q)$). We report the dependence of m_f on the initial overlap $m_0(q)$ for various values of K (50, first row; 200, second row; 500, third row), the number of examples per class M (10, left; 50, center; 200, right), and the dilution parameter d (0, blue squares; 0.5, yellow ones). The network size is fixed to $N = 1000$. The results are averaged over 500 different realizations of the couplings matrix for each point.

d lead to the m_f vs m_0 curves of the two models (with and without dilution) crossing. This indicates that there is a value of r for which the generalization capabilities of the diluted model surpass those of the non-diluted one. The situation is evident in the case $K = 250$ and $M = 200$: there is a (relatively) wide region of the quality parameter where the final magnetization of the diluted model is close to 1, thus signaling that the system (almost) correctly reproduces the hidden archetype associated with that data point.

As a final analysis, we fix the information load $\alpha = 0.1, 0.4$ and the number of examples per class $M = 50, 100, 200$, span the values of $r \in [0.5, 1]$ and $d \in [0, 1]$ and check the effects of dilution on the generalization capabilities of the network after thermalization towards fixed points of the neural dynamics. To do this, we consider the “network gain” $\delta(d, r)$ of the final Mattis magnetization at

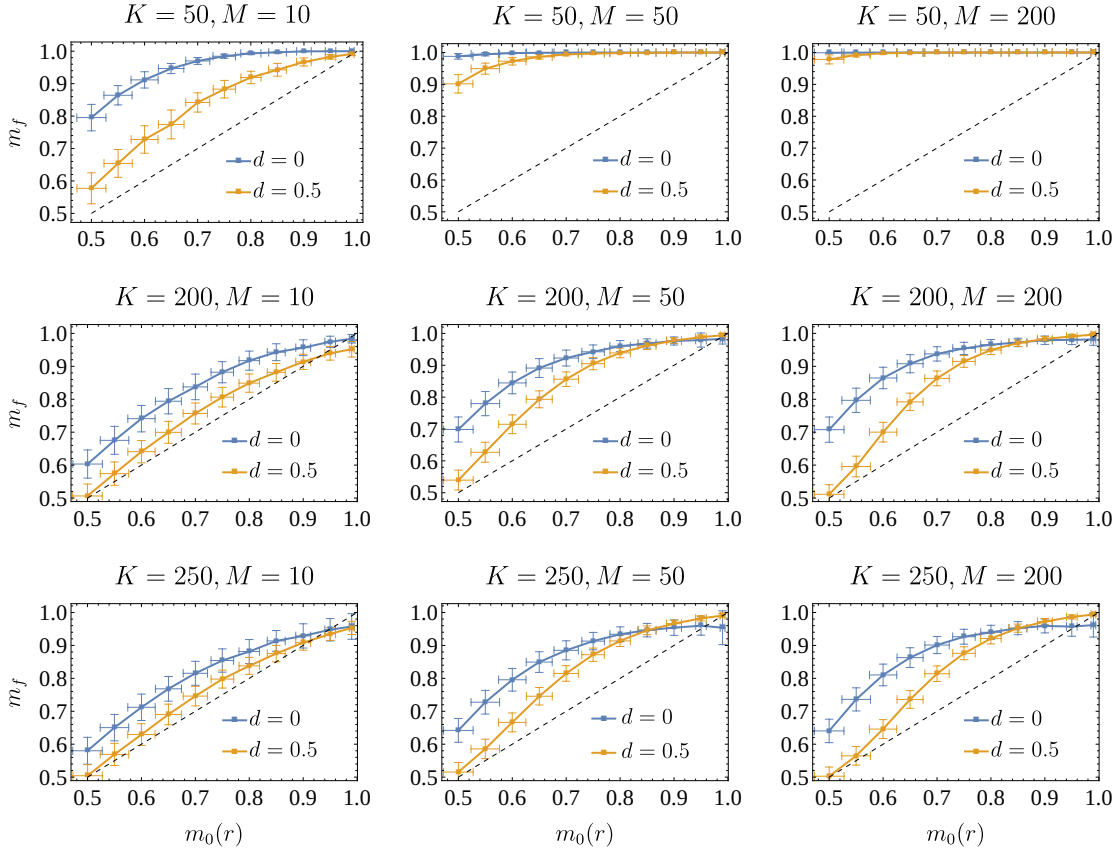


Figure 10. Generalization in the unsupervised setting. The plots report the results of the pattern attractiveness, namely the final magnetization m_f under the relaxation to fixed points of the neural dynamics (2.1) starting from a validation example (with initial magnetization $m_0(r)$). We report the dependence of m_f on the initial overlap $m_0(r)$ for various values of K (50, first row; 200, second row; 250, third row), the number of examples per class M (10, left; 50, center; 200, right), and the dilution parameter d (0, blue squares; 0.5, yellow ones). The network size is fixed to $N = 1000$. The results are averaged over 500 different realizations of the couplings matrix for each point.

dilution d w.r.t. the case without dilution. In formula:

$$\delta(d, r) = \frac{m_f(d, r) - m_f(0, r)}{m_f(0, r)}. \quad (6.1)$$

The results are reported in Fig. 11. In agreement with the analysis reported in Fig. 10, we see that, at low load ($\alpha = 0.1$) the effect of dilution on generalization capabilities is (in the best case) irrelevant, as the majority of points in the heat map exhibits zero gain in the final magnetization after the dilution is switched on. Moreover, at very poor quality dataset ($r \sim 0.5$), dilution results in a strong reduction of the reconstruction capabilities of the network, with a loss of at most 50% w.r.t. non-diluted case. Thus, again, if the number of categories in the dataset is low, the introduction of blank entries in the training examples constitute an obstruction to pattern reconstruction, and this behavior is observed even increasing the number of examples per class. In contrast, the high-load case ($\alpha = 0.4$) exhibits a qualitatively different situation. Although in low quality and large dilution, dilution still has a harmful

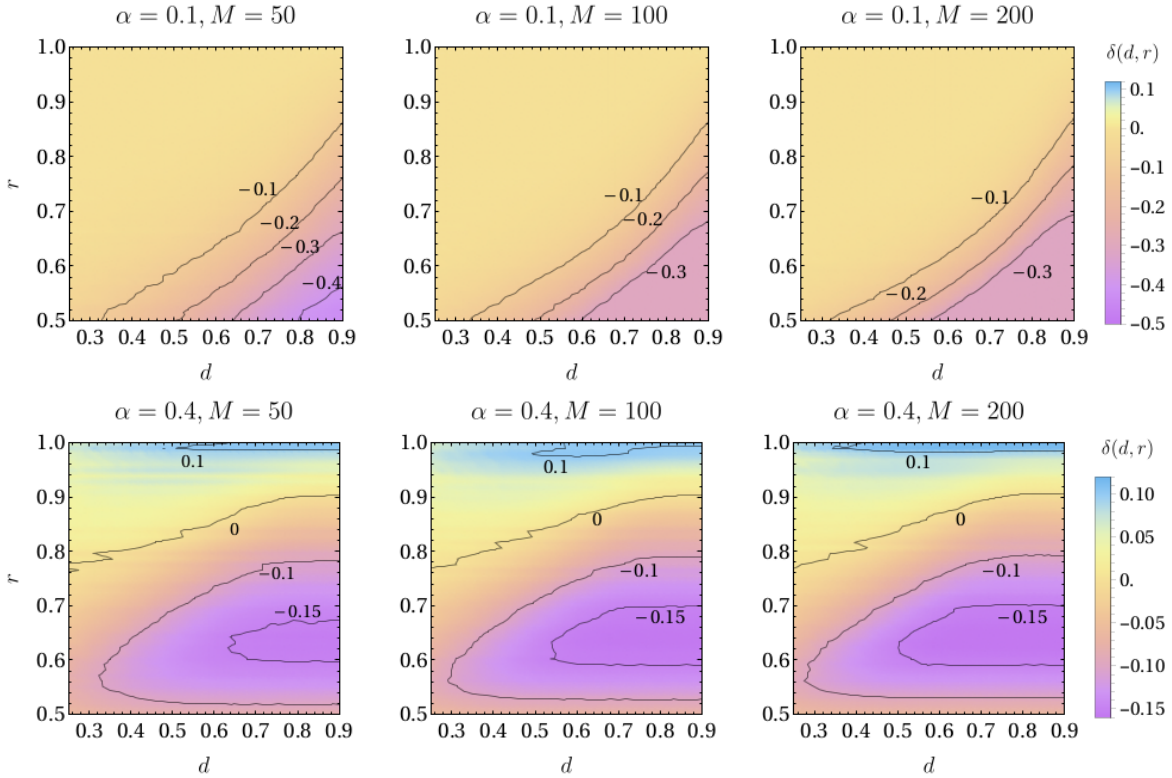


Figure 11. Generalization in the unsupervised setting in the (r, d) plane. The plots report the results of the pattern attractiveness, namely the final magnetization m_f under the relaxation to fixed points of the neural dynamics (2.1) starting from a validation example. We report the dependence of m_f on the dilution parameter d and the dataset quality r , for $\alpha = 0.1$ (first row) and $\alpha = 0.4$ (second row), and $M = 50$ (left column), $M = 100$ (center column) and $M = 200$ (right column). The black solid lines are the level curve in the heat maps. The network size is fixed to $N = 1000$. The results are collected 20 different realizations of the couplings matrix.

effect on generalization capabilities, for (very) high quality datasets (with $r \in [0.9, 1.0]$) the presence of blank entries in the training examples leads to a gain of around 10% in the final magnetization, and it improves with the number of points per class M .

6.1 An experiment with a structured dataset

As a last experiment unveiling the role of the dilution in the unsupervised Hopfield setting, we consider the case of a structured dataset. Recalling that the benign effects of diluting the training examples is manifest at high load, we should take into account a dataset with a large number of classes, if compared to the native size of the patterns. In order to explore this regime with a structured dataset, we consider as ground-truths a mixed set of Chinese characters and Japanese ideograms (drawn from Hiragana, Katakana and Kanji characters). In this wide range of possibilities, we choose 250 characters and generate Boolean representations of the selected ideograms as 25×25 matrices which will play the role of ground-truths. A sample of these patterns is reported in Fig. 12. In this way, $N = 625$ and $K = 250$, so that $\alpha = 0.4$.



Figure 12. Ten (out of 250) characters used as ground truths in the experiment.

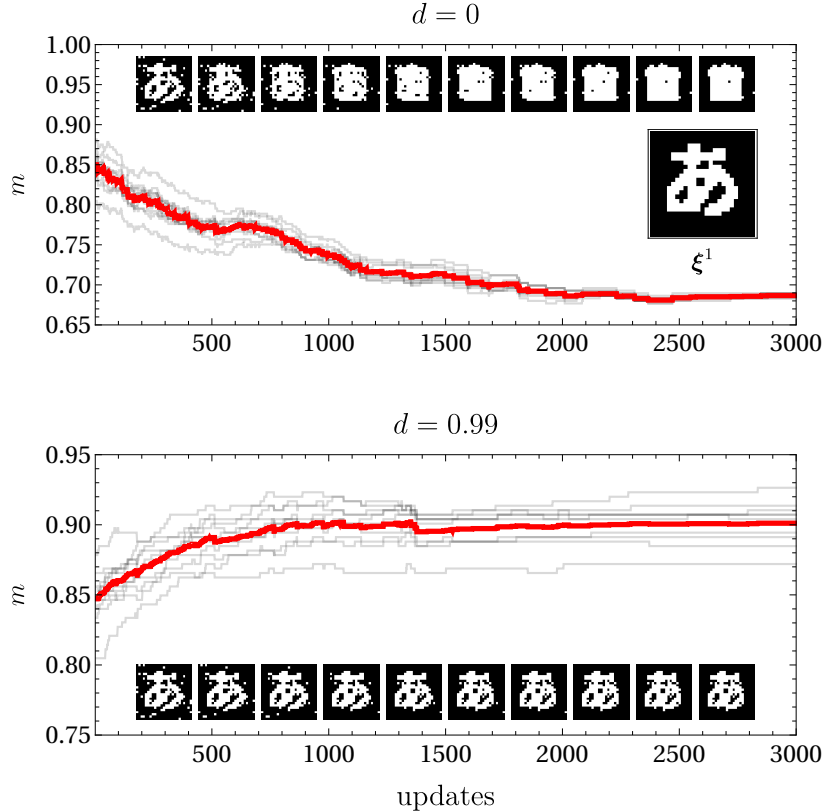


Figure 13. Effectiveness of strong dilution in the structured case. The plots show the effects of a strong dilution applied to the training examples used to generate the unsupervised Hebbian matrix. In both cases ($d = 0$, upper plot; $d = 0.99$, lower plot) we input the *same* validation example (which is a corrupted version of the ground-truth ξ^1 reported as inset in the upper plot). Then, we let the system converge to a fixed point of the neural dynamics (2.1). At each time step n , we compute the value of the Mattis magnetization $m = \frac{1}{N} \sum_i \sigma_i^{(n)} \xi_i^1$. We performed the same experiment for 10 different initial conditions, reporting the evolution of the magnetization in each run (gray solid lines) and the related average magnetization (red solid curve). We also collect snapshots of the network configurations at a distance of 300 updates (insets in both plots). The parameters are set as $N = 625$, $K = 250$, $r = 0.85$, $M = 100$.

Once the ground-truths are available, we generate a training dataset corrupting the patterns with a multiplicative Bernoulli noise with quality r and dilution d . In this experiment, the generated examples per class are $M = 100$ with quality $r = 0.85$, and we compare the cases with $d = 0$ (no dilution) and $d = 0.99$. Then, we provide the network with test examples as we did in the estimation of generation capabilities (that is, examples with the same quality as the training set, but *without* diluting the entries)

and let the system evolve towards a fixed point with deterministic Glauber dynamics (2.1).⁷ The Hebbian networks built with non-diluted and diluted training examples are fed with the same initial conditions. At each step of dynamics, we collect both the value of the magnetization corresponding to the associated ground-truth, and snapshots of the network configurations. The results are reported in Fig. 13.

In the case without dilution, the magnetization of the network configuration with the corresponding ground-truth decreases over time, and starting from an initial configuration with $m = r$ (in average) at step 0 with the pattern, the system relaxes toward a final state with lower correlation with the ground-truth. This is confirmed by looking at the snapshots of the network configuration: the system completely loses the real structure of the test example, and relaxes towards a final configuration characterized by a large “blob” of active pixels in the center of the matrix (this is a strongly attractive configuration even by varying M and r , and clearly corresponds to a spurious state involving different patterns). Nevertheless, by inserting a strong dilution in the training dataset, starting with a test example the network is able to give a better representation of the associated ground-truth, and generally the overlap with the latter and the system configuration grows along the relaxation towards the fixed point. By looking at the snapshots, we can see that the network is able to remove the noise in non-informative pixels (the dark background) while keeping memory of the structure of the associated ground-truth, thus resulting in a better reconstruction of that pattern. This experiment highlights that a strong dilution (which results in an almost-sparse coupling matrix, that is, a large fraction of entries are close to zero) is responsible for reducing the intrinsic noise in the update rule (2.1) driving the system towards spurious configurations of the patterns (which, in the structured case, are strongly correlated), thus leading to better reconstruction performances of the ground-truths underlying the training dataset.

7 Discussion and outlooks

In this work, we employed random matrix theory to investigate the properties of Hopfield neural networks starting from a stochastic synthetic data-set and facing both supervised and unsupervised settings. Using the Marchenko-Pastur theorem and introducing the AFM, we derived the asymptotic spectral distribution of the coupling matrices built on noisy and potentially sparse data. This allowed us to analytically investigate the 1-step stability, attractiveness, and generalization capabilities of stored patterns. Our findings reveal that the presence of blank or missing entries in the data can, under certain conditions, improve the performance of unsupervised Hopfield networks: this positive effect of dilution is detected especially when the data quality is high and the load is large and suggests sparsification strategies, where selective dilution may enhance generalization without sacrificing too much information. In contrast, in supervised settings, data dilution generally impairs performance, highlighting the need for careful data management in practical applications. Our theoretical results are supported by extensive numerical simulations which also demonstrate the robustness of the phenomenology when structured datasets are used. Overall, this work contributes to a deeper understanding of how sparsification and noise influence the performance of Hopfield networks, while also demonstrating how random matrix theory provides a solid theoretical framework for these studies.

Moving forward, it would be interesting to design specific dilution strategies to optimize learning and apply these insights to real-world datasets, where missing data and noise pose common challenges.

⁷Unlike the synthetic random case, we adopted a serial dynamics in order to better stress the evolution of the network in the structured scenario.

The fact that the Hebbian matrix can be recovered as the fixed point of a gradient descent algorithm with dropout represents a promising premise in this regard.

Acknowledgments

E.A. and A.F. acknowledge financial support from PNRR MUR Project PE0000013-FAIR.

E.A. acknowledges financial support from Sapienza University of Rome (RM12117A8590B3FA, RM12218169691087).

A Linking dropout and diluted datasets: a Machine Learning perspective

In this appendix, we aim to provide a relation between the operation of diluting the training dataset and the dropout technique [8] designed to avoid overfitting when training neural networks. To this aim, we revisit Hebb's rule from a Machine Learning perspective. As is well-known [45], Hebbian prescription is designed to capture spin-spin correlation within a given set of observation. Thus, we consider a sample of vectors $\mathcal{D} = \{\hat{\xi}^s\}_{s=1}^P$, where s can label independent random vectors as in the storing case (thus $P = K$), or refer to training examples in an unsupervised setting (with $P = MK$). As we are interested mainly in the empirical setting, without loss of generality we will only focus on the unsupervised setting and, since we intend to insert dilution as an external operation, we will work with undiluted training examples, namely $\hat{\xi}_i^{\mu,A} = \hat{\chi}_i^{\mu,A} \xi_i^\mu$ with $P(\hat{\chi}_i^{\mu,A} = \pm 1) = \frac{1 \pm r}{2}$. The most natural loss-function to achieve the Hebb goal reads as

$$\mathcal{L}(\mathbf{J}) = \frac{1}{2KM} \sum_{\mu,A=1}^{K,M} \|\mathbf{J} - \hat{\xi}^{\mu,A}(\hat{\xi}^{\mu,A})^T\|_{UF}^2 = \frac{1}{2KM} \sum_{\mu,A=1}^{K,M} \sum_{i,j=1}^N (J_{i,j} - \hat{\xi}_i^{\mu,A} \hat{\xi}_j^{\mu,A})^2,$$

with $\|\cdot\|_{UF}$ being the (unnormalized) Frobenius norm. The optimization task can be solve by means of gradient flow:

$$\dot{J}_{i,j} = -\partial_{J_{i,j}} \mathcal{L}(\mathbf{J}) = \frac{1}{KM} \sum_{\mu,A=1}^{K,M} \hat{\xi}_i^{\mu,A} \hat{\xi}_j^{\mu,A} - J_{i,j}.$$

The first contribution on the r.h.s. is the empirical expectation of the spin-spin correlation evaluated on the training set \mathcal{D} , while the second term plays the role of a regularization term (yielding to exponential decay of the network weights). Clearly, the fixed point of the gradient flow leads immediately to $\mathbf{J} = (KM)^{-1} \mathbf{X}^{\text{ex}}(\mathbf{X}^{\text{ex}})^T$,⁸ where (following the notation adopted in Subsec. 2.2) \mathbf{X}^{ex} is the $N \times KM$ matrix with the training examples on the columns. For our concerns, it will be helpful to consider the discretized version of the gradient flow, namely

$$\Delta J_{ij}^{(k)} = -\epsilon \partial_{J_{i,j}} \mathcal{L}(\mathbf{J}) = \frac{\epsilon}{KM} \sum_{\mu,A=1}^{K,M} \hat{\xi}_i^{\mu,A} \hat{\xi}_j^{\mu,A} - \epsilon J_{i,j}^{(k-1)},$$

with $\Delta J_{ij}^{(k)}$ being the update of the network weights at training time k , and ϵ is the learning rate. Because of the simplicity of the training equations, we can recast everything in terms of the coupling

⁸Notice that the choice of the loss function as the empirical squared error leads to a different normalization factor in the definition of the Hebbian coupling matrix. This is however not a problem, since we only deals with zero-temperature dynamics. In the statistical-mechanical setting, this would only lead to a trivial rescaling of the temperature in the high-storage regime.

matrix itself at time k . Specifically:

$$\begin{aligned} J_{i,j}^{(k)} &= \frac{\epsilon}{KM} \sum_{\mu,A=1}^{K,M} \hat{\xi}_i^{\mu,A} \hat{\xi}_j^{\mu,A} + (1-\epsilon) J_{i,j}^{(k-1)} = \frac{\epsilon}{KM} \sum_{s=0}^{k-1} (1-\epsilon)^s \cdot \sum_{\mu,A=1}^{K,M} \hat{\xi}_i^{\mu,A} \hat{\xi}_j^{\mu,A} + (1-\epsilon)^k J_{i,j}^{(0)} = \\ &= \frac{1}{KM} [1 - (1-\epsilon)^k] \sum_{\mu,A=1}^{K,M} \hat{\xi}_i^{\mu,A} \hat{\xi}_j^{\mu,A} + (1-\epsilon)^k J_{i,j}^{(0)}. \end{aligned}$$

Since $0 < \epsilon < 1$, taking the $k \rightarrow \infty$ limit immediately leads to $J_{i,j}^{(\infty)} = \frac{1}{KM} \sum_{\mu,A} \hat{\xi}_i^{\mu,A} \hat{\xi}_j^{\mu,A}$, regardless of the initial condition $\mathbf{J}^{(0)}$. Thus, the Hebbian coupling matrix is the fixed point of the gradient descent algorithm with loss function \mathcal{L} .

In order to link the dilution of training examples with the dropout technique, we slightly modify the previous algorithm implementing the following requirements: *i*) we present a single training example per update, and the whole training dataset is presented just once (thus, the total number of updates will be $k_{\max} = KM$); *ii*) we use a cooling schedule $\epsilon = \epsilon_k = \frac{\epsilon_0}{1+\epsilon_0 k}$ (this is just for computational convenience, however has turned out to be effective in unlearning schemes, see for example [23]). With these ingredients, the training equations become

$$J_{i,j}^{(k)} = \left(1 - \frac{\epsilon_0}{1 + \epsilon_0 k}\right) J_{i,j}^{(k-1)} + \frac{\epsilon_0}{1 + \epsilon_0 k} \hat{\xi}_i^k \hat{\xi}_j^k,$$

with $k = 1, \dots, KM$ and using $\hat{\xi}_i^k$ instead of $\hat{\xi}_i^{\mu,A}$ for the sake of clarity.⁹ Expressing again the k -th value of the coupling matrix in terms of the initial condition and setting $k = k_{\max} = KM$, we have

$$J_{i,j}^{(\infty)} = J_{i,j}^{(KM)} = \frac{\epsilon_0}{1 + \epsilon_0 KM} J_{i,j}^{(0)} + \frac{\epsilon_0}{1 + \epsilon_0 KM} \sum_{\mu,A=1}^{K,M} \hat{\xi}_i^{\mu,A} \hat{\xi}_j^{\mu,A}.$$

Now, if we set $\mathbf{J}^{(0)} = 0$, $\epsilon_0 = \frac{\gamma}{KM}$ with $1 \ll \gamma \ll KM$, we have $J_{i,j}^{(\infty)} \approx \frac{1}{KM} \sum_{\mu,A=1}^{K,M} \hat{\xi}_i^{\mu,A} \hat{\xi}_j^{\mu,A}$. The reason for choosing this version of the gradient descent is that dropout can be easily implemented in this setting. To do this, we apply the silencing mechanism *only* on the data-dependent part of the algorithm, as the contribution involving the $J_{i,j}^{(k)}$ will only cause a (slow) decay of the network weights. Furthermore, we assume that the diagonal entries of the coupling matrix remain set to zero throughout the entire training procedure. Thus, calling $\theta_{i,j}^{(k)}$ a set of i.i.d. $\text{Ber}(p)$, the dropout gradient descent reads as

$$J_{i,j}^{(k)} = \left(1 - \frac{\epsilon_0}{1 + \epsilon_0 k}\right) J_{i,j}^{(k-1)} + \frac{\epsilon_0}{1 + \epsilon_0 k} \theta_{i,j}^{(k)} \hat{\xi}_i^k \hat{\xi}_j^k.$$

In order to maintain the symmetry of the coupling matrix,¹⁰ the most natural choice is that assume that the $\theta_{i,j}^{(k)}$ are factorized in the product of two $\text{Ber}(1-d)$, namely $\theta_{i,j}^{(k)} = \theta_i^{(k)} \theta_j^{(k)}$ with $P(\theta_i^{(k)} = 0) = d = 1 - \sqrt{p}$. In this way, $\theta_{i,j}^{(k)} \hat{\xi}_i^k \hat{\xi}_j^k = (\theta_i^{(k)} \hat{\xi}_i^k) (\theta_j^{(k)} \hat{\xi}_j^k) = \xi_i^k \xi_j^k$, where we defined $\xi_i^k = \theta_i^{(k)} \hat{\xi}_i^k$. Along the same lines, the final value of the coupling matrix will be $J_{i,j}^{(\infty)} \approx \frac{1}{KM} \sum_{\mu,A=1}^{K,M} \xi_i^{\mu,A} \xi_j^{\mu,A}$, where the stored vectors are now the $\xi^{\mu,A}$. Recalling that $\hat{\xi}^{\mu,A} = \chi_i^{\mu,A} \xi_i^{\mu,A}$ and that, in this setting $k \equiv (\mu, A)$, we have $\chi_i^{\mu,A} = \theta_i^{\mu,A} \hat{\chi}_i^{\mu,A} \xi_i^{\mu,A} = \chi_i^{\mu,A} \xi_i^{\mu,A}$ upon identifying $\chi_i^{\mu,A} = \theta_i^{\mu,A} \hat{\chi}_i^{\mu,A}$. It is now straightforward to notice that the $\chi_i^{\mu,A}$ have the same statistics given in Eq. (2.4) used for defining the diluted training examples. Hence, the relation between the dropout and the framework defined in Sec. 2.2 is finally fulfilled.

⁹We stress that presenting a single example per update is an extreme version of the mini-batch gradient descent, where spin-spin correlations are computed point-wisely: thus, we do not normalize the updates by $(KM)^{-1}$.

¹⁰This is crucial for ensuring the detailed balance principle to hold.

B Proofs

In this appendix, we collect the proofs of the propositions used in the main text. We start recalling the Marchenko-Pastur Theorem, see [47] for a proof.

Theorem 1 (Marchenko-Pastur Theorem). *Let $\mathbf{X} = \mathbf{X}^{(N)}$ be a sequence $N \times K$ real matrices, with $\lim_{N \rightarrow \infty} K/N = \alpha \in (0, \infty)$, and such that, for each N , its entries $X_{i,\mu}^{(N)}$ are i.i.d. centered random variables with variance $\sigma^2 < +\infty$, and $\exists \{\eta_N\}_N$ such that*

$$\eta_N \rightarrow 0 \quad \text{and} \quad X_{i,\mu}^{(N)} \leq \eta_N \sqrt{N}, \quad \forall N, i, \mu. \quad (\text{B.1})$$

Let $\mathbf{S}_N = \frac{1}{K} \mathbf{X}^{(N)} \mathbf{X}^{(N)T}$ and $\mu_{\mathbf{S}}$ the empirical distribution of its eigenvalues:

$$\mu_{\mathbf{S}}(x) = \frac{1}{N} \#\{j \leq N : \lambda_j^{\mathbf{S}} < x\}. \quad (\text{B.2})$$

Then, for $N \rightarrow \infty$, $\mu_{\mathbf{S}}$ converges to a distribution $MP(\alpha, \sigma^2)$ with probability measure

$$\mu_{MP}(A) = \begin{cases} (1 - \alpha) \mathbf{1}_{0 \in A} + \alpha \mu_{bulk}(A), & \text{if } 0 \leq \alpha < 1 \\ \alpha \mu_{bulk}(A), & \text{if } \alpha \geq 1 \end{cases},$$

where

$$d\mu_{bulk}(x) = \frac{1}{2\pi\sigma^2} \frac{\sqrt{(\lambda_+ - x)(x - \lambda_-)}}{x} \mathbf{1}_{x \in [\lambda_-, \lambda_+]} dx,$$

and $\lambda_{\pm} = \sigma^2(1 \pm \sqrt{1/\alpha})^2$.

In the following we will always retain a setting $\alpha < 1$ and we will say that a random variable Z has a *shifted Marchenko-Pastur* law $MP(\alpha, \sigma^2, s)$ with shift s iff $Z - s \sim MP(\alpha, \sigma^2)$.

B.1 Proof of Prop. 1

Proof. Recalling $\mathbf{\Gamma} = \frac{1}{N} \mathbf{X} \mathbf{X}^T$, where \mathbf{X} is a $N \times K$ random matrix such that $\mathbf{X}_{i,\mu} = \xi_i^\mu$ are i.i.d. $Rad(0)$ random variables, and $K/N \rightarrow \alpha \in (0, 1)$, in the thermodynamic limit we can write $\mathbf{\Gamma} = \frac{1}{K} \sqrt{\alpha} \mathbf{X} \sqrt{\alpha} \mathbf{X}^T$. Then, $\mathbf{\Gamma}$ satisfies the hypothesis of Marchenko-Pastur theorem, since $\mathbb{E}[\sqrt{\alpha} \xi_i^\mu] = 0$ and $\mathbb{E}[(\sqrt{\alpha} \xi_i^\mu)^2] = \alpha$, hence the empirical distribution of the eigenvalues of $\mathbf{\Gamma}$ converges to a $MP(\alpha, \alpha)$. \square

In Fig. 14, we reported the comparison between the empirical spectral distributions for various values of α and its limiting distribution. As also remarked in the main text, also the supervised setting falls into the class of covariance matrices covered by the Prop. 14 (with a suitable redefinition of the scale parameter in the Marchenko-Pastur distribution). Hence, the proof follows the same lines as before. In Fig. 15, we again provide a comparison between the empirical spectral distributions and their limiting ones for various values of the control parameters r and d at $\alpha = 0.1$ and $M = 50$. As is clear, the theoretical distribution is consistent with the numerical results. In both cases, the theoretical results are robust even for relatively small sizes of the networks ($N \sim 10^2$).

B.2 Proof of Prop. 3

Proof. Recall that the explicit expression of the Hebbian kernel in the unsupervised setting reads as

$$\Gamma_{i,j}^u = \frac{1}{N} \sum_{\mu} \left(\frac{1}{M} \sum_A \chi_i^{\mu,A} \chi_j^{\mu,A} \right) \xi_i^\mu \xi_j^\mu. \quad (\text{B.3})$$

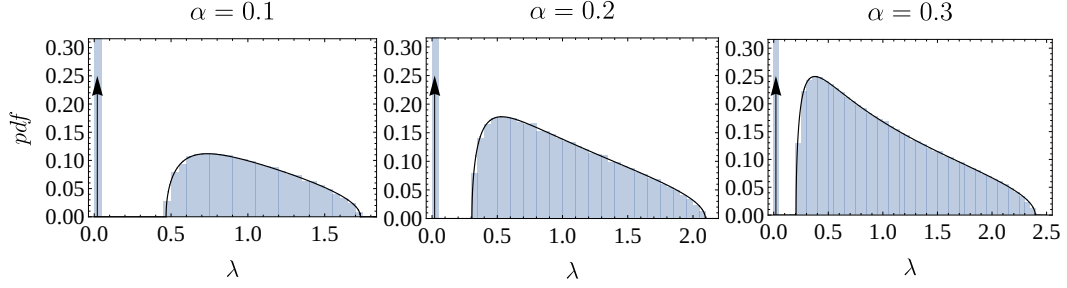


Figure 14. Histogram of the spectral distribution of Γ when $N = 1000$, for different values of α , against the analytical formula obtained by Proposition 1. The empirical distribution is realized by collecting the eigenvalues of a sample of 100 different realizations of the Hebbian matrices.

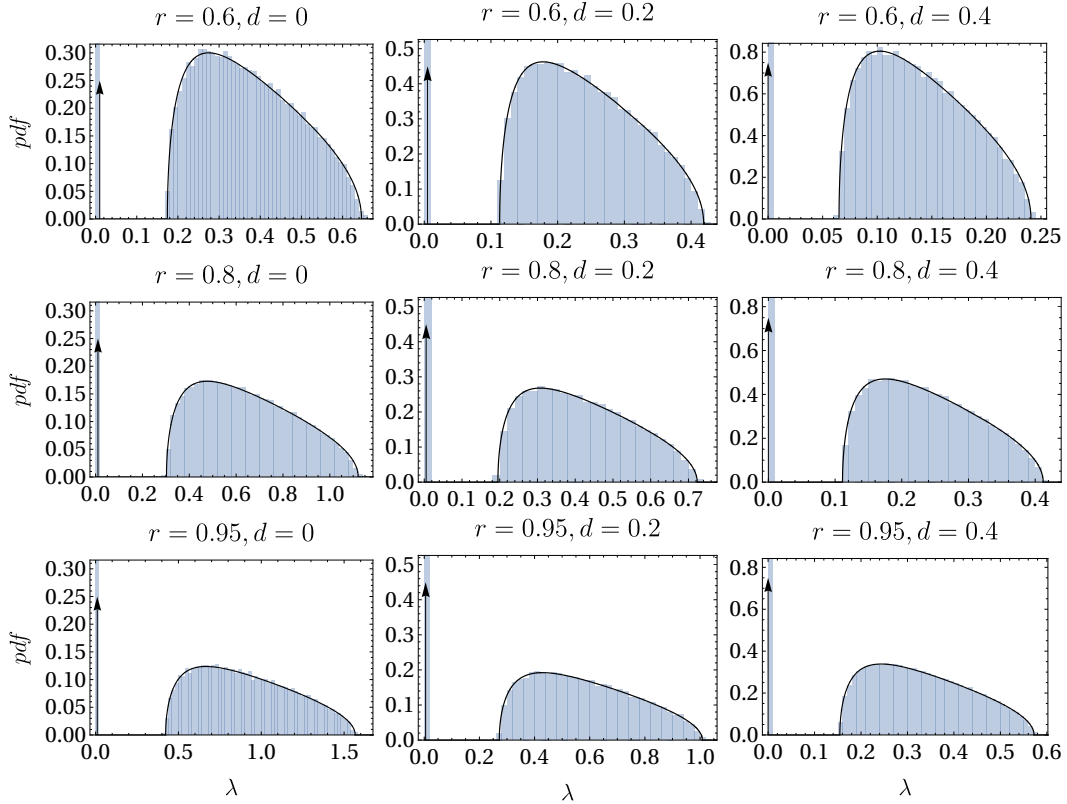


Figure 15. Histogram of the spectral distribution of Γ^s when $N = 1000$, $\alpha = 0.1$ and $M = 50$, for different values of r and d . The empirical distribution is realized by collecting the eigenvalues of a sample of 100 different realizations of the Hebbian matrices.

By virtue of the AFM (see App. C.2) and recalling that $(\xi_i^\mu)^2 = 1$, we can write (see also Eq. (C.5))

$$\Gamma_{i,j}^u = \frac{1}{N} \sum_{\mu} \phi_i^\mu \phi_j^\mu \xi_i^\mu \xi_j^\mu + \delta_{ij} \frac{1}{N} \sum_{\mu} \left(\frac{1}{M} \sum_A (\chi_i^{\mu,A})^2 - (\phi_i^\mu)^2 \right),$$

which is again the sum of a Wishart Matrix and a diagonal one. Using the strong law of large numbers, the diagonal can be evaluated straightforwardly in the thermodynamic limit, and it converges to

$$\frac{1}{N} \sum_{\mu} \left(\frac{1}{M} \sum_A (\chi_i^{\mu,A})^2 - (\phi_i^{\mu})^2 \right) \rightarrow \alpha(1 - d - \sigma^u(r, d, M)),$$

with $\sigma^u(r, d, M) = \mathbb{E}[(\phi_i^{\mu})^2]$. Proceedings as in App. C.2, we can straightforwardly evaluate

$$\begin{aligned} \sigma^u(r, d, M) &= \mathbb{E}[(\phi_i^{\mu})^2] = \sqrt{\mathbb{E}[(\phi_i^{\mu} \phi_j^{\mu})^2]} = \sqrt{\mathbb{E}\left[\left(\frac{1}{M} \sum_{A=1}^M \chi_i^{\mu,A} \chi_j^{\mu,A}\right)^2\right]} = \\ &= \sqrt{\frac{1}{M^2} \left(M \mathbb{E}[(\chi_i^{\mu,A})^2] + M(M-1) (\mathbb{E} \chi_i^{\mu,A})^2 \right)} = \\ &= \sqrt{(1-d)^4 r^4 + (1-d)^2 \frac{1 - (1-d)^2 r^4}{M}}. \end{aligned}$$

As for the contribution involving the Wishart matrix, we notice again that its factors are centered and with finite variance, hence its easy to show that the limiting spectral distribution is a $MP(\alpha, \alpha\sigma^u(r, d, M))$. Putting all pieces together, the limiting spectral distribution of the Hebbian kernel in the unsupervised setting (within the AFM) is finally $MP(\alpha, \alpha\sigma^u(r, d, M), \alpha(1 - d - \sigma^u(r, d, M)))$, which concludes the proof. \square

A comparison between the empirical spectral distributions of the Hebbian kernel in the unsupervised setting and the limiting one derived by virtue of the AFM is shown in Fig. 16. Some comments are in order here: first, even at relatively low number of examples per class M , there is a substantial agreement of the primary bulk of the limiting spectral distribution with the numerical results; clearly, again the secondary bulk – also present in the Gaussian scenario – is still approximated with a δ -peak, although the theoretical results accounts for its location. Further, increasing the dilution parameter d at fixed M (left to right in each plot), the AFM provides a less accurate predictions for the empirical spectral distribution (this is however not surprising, as high values of the dilution results in a lower effective number of examples contributing in the random sums $\frac{1}{M} \sum_{A=1}^M \chi_i^{\mu,A} \chi_j^{\mu,A}$). Despite this, in general the theoretical results given by AFM provides a good starting point to investigate the algebraic properties of the Hebbian kernel in the unsupervised setting, and hence the retrieval capabilities of the related Hopfield network.

B.3 Proof of Prop. 4

Before detailing the proof of Prop. 4, we give a definition for the first three moments of the shifted Marchenko-Pastur distribution $MP(\alpha, \alpha\sigma^2, s)$, allowing us to lighten the notations.

Definition 5. Let $\lambda \sim MP(\alpha, \alpha\sigma^2, s)$, then we define:

- $\kappa^1(\alpha, \sigma^2, s) = \mathbb{E}[\lambda] = \alpha\sigma^2 + s;$
- $\kappa^2(\alpha, \sigma^2, s) = \mathbb{E}[\lambda^2] = \alpha(1 + \alpha)(\sigma^2)^2 + 2\alpha\sigma^2 s + s^2;$
- $\kappa^3(\alpha, \sigma^2, s) = \mathbb{E}[\lambda^3] = \alpha(1 + 3\alpha + \alpha^2)(\sigma^2)^3 + 3\alpha(1 + \alpha)(\sigma^2)^2 s + 3\alpha\sigma^2 s^2 + s^3.$

We are now ready to prove Prop. 4.

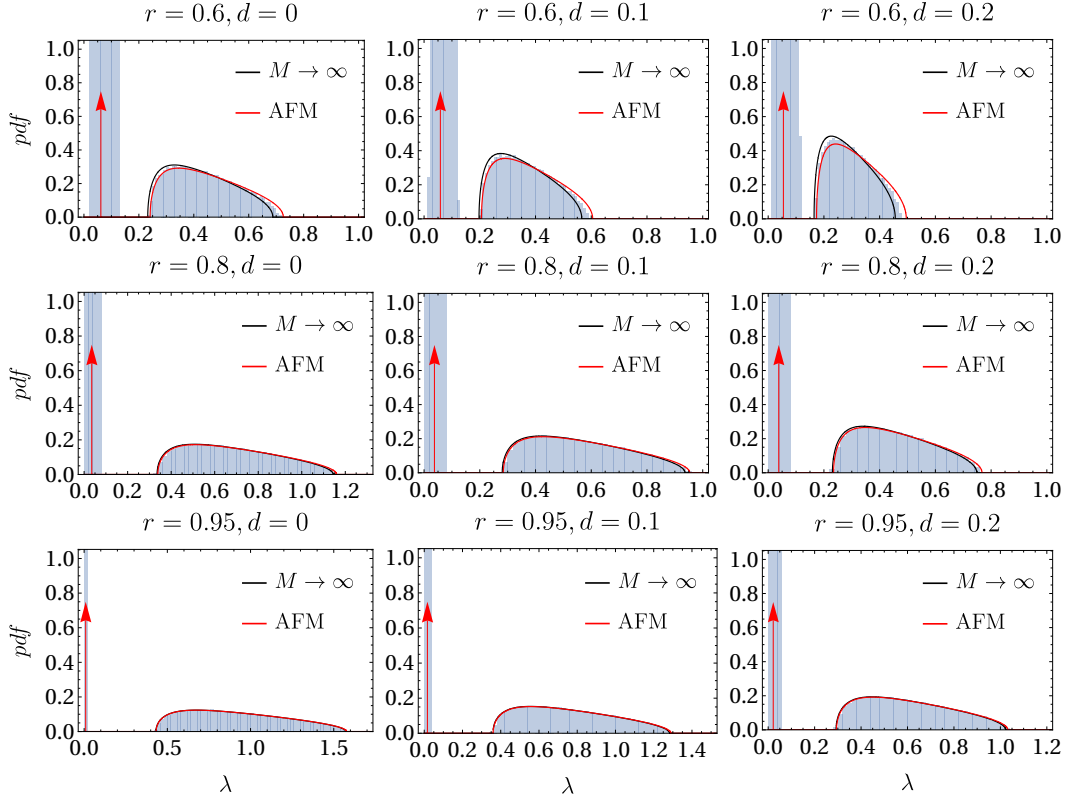


Figure 16. Histogram of the spectral distribution of Γ^u when $N = 1000$, $\alpha = 0.1$ and $M = 50$, for different values of r and d . The empirical distribution is realized by collecting the eigenvalues of a sample of 200 different realizations of the Hebbian matrices. For the theoretical distributions, we only plotted the location of the δ peak for the AFM approximation.

Proof.

$$\begin{aligned} \mu_1^{s/u} &= \frac{1}{NK} \mathbb{E}_{\boldsymbol{\eta}} \sum_{i\mu j} \Gamma_{ij}^{s/u} \eta_j \xi_i^\mu \xi_j^\mu = \frac{p}{\alpha N} \text{Tr} \Gamma^{s/u} \boldsymbol{\Gamma} = \frac{p}{2\alpha N} (\text{Tr}(\boldsymbol{\Gamma}^{s/u})^2 + \text{Tr} \boldsymbol{\Gamma}^2 - \text{Tr}(\boldsymbol{\Gamma}^{s/u} - \boldsymbol{\Gamma})^2) \\ &\xrightarrow{TDL} \frac{p}{2\alpha} (\mathbb{E}[\lambda_{\boldsymbol{\Gamma}^{s/u}}^2] + \mathbb{E}[\lambda_{\boldsymbol{\Gamma}}^2] - \mathbb{E}[\lambda_{\boldsymbol{\Gamma} - \boldsymbol{\Gamma}^{s/u}}^2]), \end{aligned}$$

where TDL stands for the thermodynamic limit ($N \rightarrow \infty$ and $K/N \rightarrow \alpha$) and where we used the cyclicity of the trace together with $\mathbf{A}\mathbf{B} + \mathbf{B}\mathbf{A} = (\mathbf{A}^2 + \mathbf{B}^2 - (\mathbf{A} - \mathbf{B})^2)$. Similarly

$$\begin{aligned} \mu_2^{s/u} &= \frac{1}{NK} \mathbb{E}_{\boldsymbol{\eta}} \sum_{i\mu jk} \Gamma_{ij}^{s/u} \Gamma_{ik}^{s/u} \eta_j \eta_k \xi_i^\mu \xi_k^\mu = \frac{1-p^2}{N} \text{Tr} \boldsymbol{\Gamma}^2 + \frac{p^2}{\alpha N} \text{Tr}(\boldsymbol{\Gamma}^{s/u})^2 \boldsymbol{\Gamma} \\ &= \frac{1-p^2}{N} \text{Tr}(\boldsymbol{\Gamma}^{s/u})^2 + \frac{p^2}{6\alpha N} (\text{Tr}(\boldsymbol{\Gamma}^{s/u} + \boldsymbol{\Gamma})^3 + \text{Tr}(\boldsymbol{\Gamma}^{s/u} - \boldsymbol{\Gamma})^3 - 2\text{Tr} \boldsymbol{\Gamma}^2) \\ &\xrightarrow{N \rightarrow \infty} (1-p^2) \mathbb{E}[\lambda_{\boldsymbol{\Gamma}^{s/u}}^2] + \frac{p^2}{6\alpha} (\mathbb{E}[\lambda_{\boldsymbol{\Gamma} - \boldsymbol{\Gamma}^{s/u}}^3] + \mathbb{E}[\lambda_{\boldsymbol{\Gamma} + \boldsymbol{\Gamma}^{s/u}}^3] - 2\mathbb{E}[\lambda_{\boldsymbol{\Gamma}}^3]), \end{aligned}$$

where we used that $\mathbf{A}^2\mathbf{B} + \mathbf{A}\mathbf{B}\mathbf{A} + \mathbf{B}\mathbf{A}^2 = \frac{1}{2}[(\mathbf{A} + \mathbf{B})^3 + (\mathbf{B} - \mathbf{A})^3 - 2\mathbf{B}^3]$ and, due to the cyclicity of the trace, $\text{Tr}(\mathbf{A}^2\mathbf{B} + \mathbf{A}\mathbf{B}\mathbf{A} + \mathbf{B}\mathbf{A}^2) = 3\text{Tr} \mathbf{A}^2\mathbf{B}$. The problem now reduces to calculating the asymptotic

distribution for each contributions in the previous equations. Now, from the propositions in Sec. 3 we already know that

$$\lambda_{\Gamma} \sim MP(\alpha, 1, 0), \quad \lambda_{\Gamma^s} \sim MP(\alpha, \sigma^s, 0), \quad \lambda_{\Gamma^u} \sim MP(\alpha, \sigma^u, s^u).$$

Now, both $\mu_1^{s/u}$ and $\mu_2^{s/u}$ depends on the matrix $\frac{1}{N} \text{Tr}(\Gamma^{s/u} - \Gamma)^2$, namely the normalized Frobenius norm of the Hebbian kernel in the (un)supervised setting w.r.t. the storing case. This quantity has been already exploited in Sec. 4 when dealing with the validity of the empirical models. In both cases, we used the AFM to see that

$$\lambda_{\Gamma - \Gamma^{s/u}} \sim MP(\alpha, \alpha \sigma_-^{s/u}, s_-^{s/u}).$$

This claim, together with the explicit forms of the scale and shift parameters $\sigma_-^{s/u}$ and $s_-^{s/u}$ are derived in App. D. It is easy to show (with analogous computations) that

$$\lambda_{\Gamma + \Gamma^{s/u}} \sim MP\left(\alpha, \alpha \sigma_+^{s/u}, s_+^{s/u}\right),$$

where

- $\sigma_+^s = \sqrt{1 + 2(1-d)^2 r^2 + \left((1-d)^2 r^2 + (1-d) \frac{1-(1-d)r^2}{M}\right)^2}$;
- $s_+^s = \alpha(1 + \sigma^s - \sigma_+^s)$;
- $\sigma_+^u = \sqrt{1 + 2(1-d)^2 r^2 + (\sigma^u)^2}$;
- $s_+^u = \alpha(1 + (1-d) - \sigma_+^u)$,

and we recall that

$$\begin{aligned} \sigma^s(r, d, M) &= (1-d) \left((1-d)r^2 + \frac{1-(1-d)r^2}{M} \right), \\ \sigma^u(r, d, M) &= \sqrt{(1-d)^4 r^4 + (1-d)^2 \frac{1-(1-d)^2 r^4}{M}}. \end{aligned}$$

Using these results, we can express $\mu_{1,2}^{s/u}$ in terms of the moments of Def. 5 and derive Eqs. (5.6-5.7). This concludes the proof. \square

C The Approximate Factorization Method

In the canonical Marchenko-Pastur Theorem, the entries of the factor matrix \mathbf{X} are assumed to be independent. Conversely, in the one-step analysis we dealt with cases (namely, the unsupervised setting) where this assumption does not hold anymore. In this appendix, we deepen the Approximate Factorization Method (AFM) – already introduced in Def. 1 – allowing to bypass mutual dependence of entries involved in the family of covariance matrices (covering the unsupervised Hebbian setting), and thus to compute the asymptotic spectral distribution. Further, we will compare the results to the benchmark approximation $M \rightarrow \infty$ extensively employed in [22, 42].

Let $M, N, K \in \mathbb{N}$, $P = KM$ and \mathbf{X} be the matrix with entries $X_{i,(\mu,A)} = \chi_i^{\mu,A} \xi_i^\mu$ for $i = 1, \dots, N$, $\mu = 1, \dots, K$, and $A = 1, \dots, M$, where $\{\chi_i^{\mu,A}\}_{i,\mu,A}$ and $\{\xi_i^\mu\}_{i,\mu}$ are, respectively, two independent classes of i.i.d. random variables with finite moments. In particular, let us assume that $\mathbb{E}\xi_i^\mu = 0$, and call $\mathbb{E}(\xi_i^\mu)^2 = \theta^2$, $\mathbb{E}\chi_i^\mu = r$ and $\mathbb{E}(\chi_i^\mu)^2 = \rho^2$. With these definitions, \mathbf{X} is a $N \times P$ matrix, and

the index μ labels a group of M columns (each with length N), whose individual element is further specified by the index A . We consider the Wishart-like ensemble of random matrices¹¹

$$\mathbf{S} = \frac{1}{P} \mathbf{X} \mathbf{X}^T. \quad (\text{C.1})$$

We will consider the spectral properties of this ensemble when $N \rightarrow \infty$ with $\lim_{N \rightarrow \infty} K/N = \alpha > 0$ fixed (the thermodynamic limit). Straightforward computations shows that $\mathbb{E} \mathbf{X}_{i,(\mu,A)} = 0$, while

$$\text{Cov}(\mathbf{X}_{i,(\mu,A)}, \mathbf{X}_{i,(\mu,B \neq A)}) = \theta^2 \rho^2 > 0,$$

which breaks statistical independence of entries of the \mathbf{X} matrix: thus, Marchenko-Pastur theorem cannot be applied.

C.1 The $M \rightarrow \infty$ limit

A first simplification in the study of Wishart-like correlation matrices occurs in the limit $M \rightarrow \infty$ (at fixed N , also referred as to the *big data* limit [22, 42]). Indeed, rewriting

$$S_{i,j} = \frac{1}{KM} \sum_{\mu=1}^K \sum_{A=1}^M X_{i,(\mu,A)} X_{j,(\mu,A)} = \frac{1}{K} \sum_{\mu=1}^K \left(\frac{1}{M} \sum_{A=1}^M \chi_i^{\mu,A} \chi_j^{\mu,A} \right) \xi_i^\mu \xi_j^\mu, \quad (\text{C.2})$$

and using the strong law of large numbers, which provides

$$\frac{1}{M} \sum_{A=1}^M \chi_i^{\mu,A} \chi_j^{\mu,A} \xrightarrow{M \rightarrow \infty} \mathbb{E}(\chi_i^{\mu,A})^2 \delta_{i,j} + \mathbb{E} \chi_i^{\mu,A} \cdot \mathbb{E} \chi_j^{\mu,A} (1 - \delta_{i,j}) = \delta_{i,j} \rho^2 + (1 - \delta_{i,j}) r^2,$$

we obtain

$$S_{i,j} = \frac{r^2}{K} \sum_{\mu=1}^K \xi_i^\mu \xi_j^\mu + \delta_{i,j} (\rho^2 - r^2) \frac{1}{K} \sum_{\mu=1}^K (\xi_i^\mu)^2.$$

In other words, in the big data limit, the Wishart-like matrix \mathbf{S} splits as the sum of an actual Wishart matrix and a diagonal one, which can be analyzed separately in the thermodynamic limit. For the diagonal contribution, again using the strong law of large numbers, we get

$$\frac{1}{K} \sum_{\mu=1}^K (\xi_i^\mu)^2 \xrightarrow{K \rightarrow \infty} \mathbb{E}(\xi_i^\mu)^2 = \theta^2.$$

Hence, the diagonal matrix converges to $\theta^2(\rho^2 - r^2)\mathbf{1}$. On the other hand, the Wishart matrix can be written as $\frac{1}{K} \mathbf{Y} \mathbf{Y}^T$ where $Y_{i,\mu} = r \xi_i^\mu$, whose entries are independent random variables with zero mean and second moment

$$\mathbb{E}(r \xi_i^\mu)^2 = r^2 \theta^2.$$

Thus, Marchenko-Pastur Theorem applies, and the empirical spectral distribution of $\frac{1}{K} \mathbf{Y} \mathbf{Y}^T$ converges to a $MP(\alpha, r^2 \theta^2)$, as $N \rightarrow \infty$. Going back to the matrix \mathbf{S} in the big data limit, the diagonal contributions only gives a shift in the eigenvalues, and the asymptotic spectral distribution is modified accordingly, leading to the distribution (recall that, in this notation, the third argument of the Marchenko-Pastur law stands for the shift)

$$MP(\alpha, r^2 \theta^2, \theta^2(\rho^2 - r^2)). \quad (\text{C.3})$$

¹¹Here, we adopted the normalization by P instead of NM as in the definition of the unsupervised (2.10), which allows us to avoid unessential rescalings of the eigenvalues.

This asymptotic is expected to fit the real distribution for large (but finite) M , yet it fails for (even relatively) small number of examples per class M . Further, adopting this limit in the unsupervised setting, it is not possible to capture essential scaling between M and the relevant parameters characterizing the training dataset. This motivates the AFM exploited in the next paragraph.

C.2 Finite (but large) M : the Approximate Factorization Method

As already stated before, the peculiarity of the unsupervised setting is due to the presence of the random sums $\frac{1}{M} \sum_{A=1}^M \chi_i^{\mu,A} \chi_j^{\mu,A}$, whose presence breaks the possibility to recover the usual Wishart setting. However, as exploited in the previous Subsection, when M is large enough, simplicifications are expected to hold and, in the big data limit, the factorization in a Wishart-type matrix (expect for a trivial shift of the eigenvalues) is reproduced. Based on this observation, and thus recover the Marchenko-Pastur Theorem 1, we assume that there is a class of i.i.d. random variables, namely $\{\phi_i^\mu\}_{i,\mu}$, such that

$$\phi_i^\mu \phi_j^\mu \approx \frac{1}{M} \sum_{A=1}^M \chi_i^{\mu,A} \chi_j^{\mu,A}, \quad \forall i \neq j \text{ and } \forall \mu. \quad (\text{C.4})$$

from which the name to the Approximate Factorization Method. An immediate observation is that the factors ϕ_i^μ are a function of the errors $\chi_i^{\mu,A}$, but clearly they are independent on patterns ξ_i^μ . Within the AFM, for $i \neq j$, the expression of $S_{i,j}$ reads as

$$S_{i,j} = \frac{1}{K} \sum_{\mu=1}^K \phi_i^\mu \phi_j^\mu \xi_i^\mu \xi_j^\mu.$$

Hence, taking in consideration also the diagonal contributions, we can rewrite the Wishart-like matrix in the form

$$\mathbf{S} = \frac{1}{K} \mathbf{\Phi} \mathbf{\Phi}^T + \text{diag} \left[\frac{1}{K} \sum_{\mu=1}^K \left(\frac{1}{M} \sum_{A=1}^M (\chi_i^{\mu,A})^2 - (\phi_i^\mu)^2 \right) (\xi_i^\mu)^2 \right], \quad (\text{C.5})$$

where $\mathbf{\Phi}$ is a $N \times K$ matrix with entries $\Phi_i^\mu = \phi_i^\mu \xi_i^\mu$. Remarkably, the matrix \mathbf{S} is again the sum of a Wishart random matrix and a diagonal matrix. Let us focus on the first contribution. Concerning the Φ_i^μ random variables, it is straightforward to notice that:

- they are i.i.d.;
- they have zero mean;
- the variance is $\text{Var}(\Phi_i^\mu) = \mathbb{E}[(\phi_i^\mu \xi_i^\mu)^2] = \mathbb{E}[(\phi_i^\mu)^2] \mathbb{E}[(\xi_i^\mu)^2] = \theta^2 \mathbb{E}[(\phi_i^\mu)^2]$.

At this level, we only need to compute $\mathbb{E}[(\phi_i^\mu)^2]$. To this aim, we observe that

$$\mathbb{E}[(\phi_i^\mu)^2]^2 \equiv \mathbb{E}[(\phi_i^\mu \phi_j^\mu)^2] = \mathbb{E} \left[\left(\frac{1}{M} \sum_{A=1}^M \chi_i^{\mu,A} \chi_j^{\mu,A} \right)^2 \right] = r^4 + \frac{\rho^4 - r^4}{M},$$

which leads to

$$\mathbb{E}[(\phi_i^\mu)^2] = \sqrt{r^4 + \frac{\rho^4 - r^4}{M}}. \quad (\text{C.6})$$

As for the diagonal part, by virtue of the strong law of large numbers and by the independence of ξ_i^μ and $\chi_i^{\mu,A}$, in the thermodynamic limit we have

$$\frac{1}{K} \sum_{\mu=1}^K \left(\frac{1}{M} \sum_{A=1}^M (\chi_i^{\mu,A})^2 - (\phi_i^\mu)^2 \right) (\xi_i^\mu)^2 \xrightarrow{K \rightarrow \infty} \theta^2 (\rho^2 - \mathbb{E}[(\phi_i^\mu)^2]),$$

where the expectation in the last line is given by Eq. (C.6). Hence, we can conclude that, in the thermodynamic limit and by virtue of the AFM, the spectral distribution of \mathbf{S} converges asymptotically to the Marchenko-Pastur distribution

$$MP\left(\alpha, \theta^2 \sqrt{r^4 + \frac{\rho^4 - r^4}{M}}, \theta^2 \left(\rho^2 - \sqrt{r^4 + \frac{\rho^4 - r^4}{M}}\right)\right). \quad (\text{C.7})$$

Clearly, the $M \rightarrow \infty$ exactly recovers the result (C.3). Although the approximated nature of the pursued method, it capture the scaling between M , r and ρ .

C.3 A counterexample at finite (but small) M

In this appendix, we give a counterexample showing that the AFM does not work at small M . Suppose, for instance, that the $\chi_i^{\mu, A}$ are i.i.d. Bernoulli random variables, and fix $M = 3$. If we could always split the sum in the expression of $S_{i,j}$ in two i.i.d. random variables we should have that, given $X \sim \text{Bin}(M = 3, p)$, there are two i.i.d. random variables Y and Z , such that $X \sim YZ$. Then, adopting the condensed notation $\mathcal{P}_X(k) = \mathcal{P}(X = k)$ we should have:

- $(1 - p)^3 = \mathcal{P}_X(0) = \mathcal{P}_Y(0) + \mathcal{P}_Z(0) - \mathcal{P}_Y(0)\mathcal{P}_Z(0) = 2\mathcal{P}_Y(0) - \mathcal{P}_Y(0)^2$;
- $3p(1 - p)^2 = \mathcal{P}_X(1) = \mathcal{P}_Y(1)\mathcal{P}_Z(1) = \mathcal{P}_Y(1)^2$;
- $3p^2(1 - p) = \mathcal{P}_X(2) = \mathcal{P}_Y(1)\mathcal{P}_Z(2) + \mathcal{P}_Y(2)\mathcal{P}_Z(1) = 2\mathcal{P}_Y(1)\mathcal{P}_Y(2)$;
- $p^3 = \mathcal{P}_X(3) = \mathcal{P}_Y(1)\mathcal{P}_Z(3) + \mathcal{P}_Y(3)\mathcal{P}_Z(1) = 2\mathcal{P}_Y(1)\mathcal{P}_Y(3)$;

where we used the fact that Z and Y must have the same support of X and, of course, that they are independent and they have the same probability distribution. The calculations above lead us to:

- $\mathcal{P}_Y(0) = 1 - \sqrt{1 - (1 - p)^3}$;
- $\mathcal{P}_Y(1) = \sqrt{3p}(1 - p)$
- $\mathcal{P}_Y(2) = \frac{\sqrt{3}}{2} p^{\frac{3}{2}}$
- $\mathcal{P}_Y(3) = \frac{p^{\frac{5}{2}}}{2\sqrt{3}(1-p)}$

But, on the other hand, being \mathcal{P}_Y a probability distribution, we are constrained by the condition:

$$1 = \sum_{i=0}^4 \mathcal{P}_Y(i) = 1 - \sqrt{1 - (1 - p)^3} + \sqrt{3p}(1 - p) + \frac{\sqrt{3}}{2} p^{\frac{3}{2}} + \frac{p^{\frac{5}{2}}}{2\sqrt{3}(1 - p)},$$

which is true if and only if $p = 0$: in this case, the factorization is not only inexact, but fails also as an approximation. The regime of applicability is clearly $M \gg 1$, in which case heuristic arguments in its favor can be carried out. For instance, when $M \gg 1$, by virtue of the Central Limit Theorem the sum $\frac{1}{M} \sum_{A=1}^M \chi_i^{\mu, A} \chi_j^{\mu, A}$ has a Gaussian behavior. Moreover, using the Delta-Method [48], one can prove that the centered and normalized product of two independent $\text{Bin}(L, p)$ converge in distribution to a Gaussian random variable when $L \rightarrow \infty$. This means that in the limit $M \rightarrow \infty$ there are two i.i.d. random variables that, for $L \rightarrow \infty$, converge to the sum above, and AFM holds.

C.4 An algebraic comment on AFM

As a side note, we make a further comment about the validity of the AFM. Let us assume generate $\chi_i^{\mu,A}$ and collect the entries $i = 1, \dots, N$ for fixed μ and A in vectors $\boldsymbol{\chi}^{\mu,A}$, lying in \mathbb{R}^N (for instance, in the Gaussian scenario $\chi_i^{\mu,A} \sim \mathcal{N}(r, \sqrt{\rho^2 - r^2})$, we would have $\boldsymbol{\chi}^{\mu,A} = \mathbf{r} + \sqrt{\rho^2 - r^2} \mathbf{z}^{\mu,A}$, with $\mathbf{r} = r(1, 1, \dots, 1)$ the mean vector and $\mathbf{z}_i^{\mu,A} \sim_{i.i.d.} \mathcal{N}(0, 1)$ isotropic perturbations around \mathbf{r}). Let us now fix $\mu = 1, \dots, K$ and generate $M < N$ ¹² vectors as before, then with large probability they will be linearly independent (since they are expressed as the sum of a constant vector \mathbf{r} and, for large N , mutually orthogonal vectors $\mathbf{z}^{\mu,A}$). Now, the random sums (with fixed μ)

$$\frac{1}{M} \sum_{A=1}^M \chi_i^{\mu,A} \chi_j^{\mu,A},$$

display a projector-like structure, namely $\frac{1}{M} \sum_{A=1}^M \boldsymbol{\chi}^{\mu,A} (\boldsymbol{\chi}^{\mu,A})^T$, where the attribute “-like” is due to the fact that the vectors are not mutually orthogonal. Indeed, even in the $N \rightarrow \infty$ limit, the angle between any pair of vectors $\boldsymbol{\chi}^{\mu,A}$ and $\boldsymbol{\chi}^{\mu,B}$ is non-zero:

$$\cos \theta(\boldsymbol{\chi}^{\mu,A}, \boldsymbol{\chi}^{\mu,B}) = \frac{\boldsymbol{\chi}^{\mu,A} \cdot \boldsymbol{\chi}^{\mu,B}}{\|\boldsymbol{\chi}^{\mu,A}\| \|\boldsymbol{\chi}^{\mu,B}\|} \underset{N \gg 1}{\approx} \frac{r^2}{\rho^2} + N^{-1/2} \sqrt{1 - \frac{r^4}{\rho^4}} z_{AB}^{\mu},$$

with $z_{AB}^{\mu} \sim \mathcal{N}(0, 1)$, since $\|\boldsymbol{\chi}^{\mu,A}\| \approx \rho \sqrt{N}$. Thus, the kernel $M^{-1} \sum_{A=1}^M \boldsymbol{\chi}^{\mu,A} (\boldsymbol{\chi}^{\mu,A})^T$ is associated, for fixed μ , with a M -dimensional subspace of \mathbb{R}^N , which we call V . Now, when introducing the AFM, we assumed that there exists a single (random) vector $\boldsymbol{\phi}^{\mu}$ exactly reproducing the statistics of $M^{-1} \sum_{A=1}^M \boldsymbol{\chi}^{\mu,A} (\boldsymbol{\chi}^{\mu,A})^T$, so that we can replace (for $i \neq j$) the kernel $\frac{1}{NM} \sum_{\mu} \sum_A \chi_i^{\mu,A} \chi_j^{\mu,A} \xi_i^{\mu} \xi_j^{\mu}$ with the simplest one $\frac{1}{N} \sum_{\mu} \phi_i^{\mu} \phi_j^{\mu} \xi_i^{\mu} \xi_j^{\mu}$. This is clearly not true in general, as $\boldsymbol{\phi}^{\mu}$ (for μ fixed) is associated with a 1-dimensional subspace of \mathbb{R}^N . However, things get simpler for high enough M , and the signature of the subspace V in the structure of the Hebbian kernel $\boldsymbol{\Gamma}^u$ can be safely neglected in this regime. To see this, let us take any vector $\mathbf{x} \in \mathbb{R}^N$ and consider $(\boldsymbol{\Gamma}^u \cdot \mathbf{x})_i = \frac{1}{N} \sum_{\mu} \xi_i^{\mu} (\frac{1}{M} \sum_{jA} \chi_i^{\mu,A} \chi_j^{\mu,A} \xi_j^{\mu} x_j)$.¹³ For a given set M of vectors $\{\boldsymbol{\chi}^{\mu,1}, \dots, \boldsymbol{\chi}^{\mu,M}\}$ and calling $v_j^{\mu} = \xi_j^{\mu} x_j$ (which is independent of the $\boldsymbol{\chi}^{\mu,A}$ vectors), we can always decompose $\mathbf{v}^{\mu} = \mathbf{v}_{\parallel}^{\mu} + \mathbf{v}_{\perp}^{\mu}$, with $\mathbf{v}_{\parallel}^{\mu} = \frac{1}{\sqrt{M}} \sum_{A=1}^M c_{\mu,A} \boldsymbol{\chi}^{\mu,A}$ and $\mathbf{v}_{\perp}^{\mu} \in V^{\perp}$, that is $\boldsymbol{\chi}^{\mu,A} \cdot \mathbf{v}_{\perp}^{\mu} = 0$ for all A . Now, different realizations of the vectors $\boldsymbol{\chi}^{\mu,A}$ translates in different decompositions, thus the coefficients $c_{\mu,A}$ are random variables depending on the $\boldsymbol{\chi}^{\mu,A}$ vectors; *ii*) since the vectors $\boldsymbol{\chi}^{\mu,A}$ are mutually independent random vectors, then so will be the coefficients $c_{\mu,A}$ (indeed, replacing for some \bar{A} the $\boldsymbol{\chi}^{\mu,\bar{A}}$ with a new vector $\tilde{\boldsymbol{\chi}}^{\mu}$ will only affect the coefficient $c_{\bar{A}}$). But now:

$$\begin{aligned} \frac{1}{NM} \sum_{jA} \chi_i^{\mu,A} \chi_j^{\mu,A} \xi_j^{\mu} x_j &= \frac{1}{NM} \sum_{jA} \chi_i^{\mu,A} \chi_j^{\mu,A} v_j^{\mu} = \frac{1}{NM} \sum_{jA} \chi_i^{\mu,A} \chi_j^{\mu,A} v_{\parallel,j}^{\mu} = \\ &= \frac{1}{NM} \left(\frac{1}{\sqrt{M}} \sum_A c_{\mu,A} \chi_i^{\mu,A} \|\boldsymbol{\chi}^{\mu,A}\|^2 + \frac{1}{\sqrt{M}} \sum_{A \neq B} c_{\mu,B} \chi_i^{\mu,A} \|\boldsymbol{\chi}^{\mu,A}\| \|\boldsymbol{\chi}^{\mu,B}\| \cos \theta_{AB} \right) \approx \\ &\approx \frac{\rho^2 - r^2}{M} \frac{1}{\sqrt{M}} \sum_A c_{\mu,A} \chi_i^{\mu,A} + \frac{r^2}{M} \sum_B \frac{c_{\mu,B}}{\sqrt{M}} \cdot \sum_A \chi_i^{\mu,A} = \frac{\rho^2 - r^2}{M} v_{\parallel,i}^{\mu} + r^2 \sum_B \frac{c_{\mu,B}}{\sqrt{M}} \cdot \frac{1}{M} \sum_A \chi_i^{\mu,A}. \end{aligned}$$

It is straightforward to notice that the only contributions carrying information about V is the first one, as we can approximate both $\sum_B c_{\mu,B} / \sqrt{M}$ and $\sum_A \chi_i^{\mu,A}$ by virtue of the CLT to get an example-free approximation, in particular $\frac{1}{M} \sum_{A=1}^M \chi_i^{\mu,A} \sim \bar{\chi}_i^{\mu}$ with $\bar{\chi}_i^{\mu}$ Gaussian-distributed. Assuming that

¹²Possibly, $1 \ll M \ll N$.

¹³The constraint $j \neq i$ only gives trivial corrections, thus can be safely omitted.

$\sum_B c_{\mu,B}/\sqrt{M}$ has some finite limit c_μ , then we would have $\frac{1}{NM} \sum_{jA} \chi_i^{\mu,A} \chi_j^{\mu,A} \xi_j^\mu x_j \approx r^2 c_\mu \bar{\chi}_i^\mu + \mathcal{O}(M^{-1})$. This finally implies

$$(\mathbf{\Gamma}^u \cdot \mathbf{x})_i \approx r^2 \sum_{\mu} \xi_i^\mu c_\mu \bar{\chi}_i^\mu + \mathcal{O}\left(\frac{\rho^2 - r^2}{M}\right).$$

Then, for M large enough, the first contribution can be neglected. On the other hand, taking a set of i.i.d. random variables $\{\phi_i^\mu\}$, and decomposing it again in the ϕ -collinear and orthogonal parts, namely $v_j^\mu = \xi_i^\mu x_i = C_\mu \phi_j^\mu + w_{j,\perp}$, we would get $\frac{1}{N} \sum_j \phi_i^\mu \phi_j^\mu \xi_j^\mu x_j = C_\mu \sigma^2 \phi_i^\mu$, where $\sigma^2 = \mathbb{E}(\phi_i^\mu)^2$. This in turn leads to

$$(\mathbf{\Gamma}^u \cdot \mathbf{x})_i \approx \sigma^2 \sum_{\mu} \xi_i^\mu C_\mu \phi_i^\mu.$$

The two approaches exhibits compatibles structure, and the latter is expected to match the whole unsupervised Hebbian kernel when $(\rho^2 - r^2)/M \ll 1$. In this sense, AFM can be interpreted as a Central Limit Theorem (although it is not proven) for projector(-like) operators, and in particular will be very useful for our concerns since both spectral properties and retrieval capabilities are directly related to quantities of the form $(\mathbf{\Gamma}^u \cdot \mathbf{x})_i$.

C.5 Time to face the reality: simulations

To conclude this Appendix, we numerically explore the validity of the AFM. Here, we assume the Gaussian scenario, namely $\xi_i^\mu \sim \mathcal{N}(0, \theta^2)$ and $\chi_i^{\mu,A} \sim \mathcal{N}(r, \rho^2 - r^2)$. This will allow us to conduct the analysis for general values θ and ρ , which in the Rademacher setting exploited in the main text are instead fixed. In Figure 17, we report the comparison between the empirical spectral distribution of a sample of Wishart-like matrices and the theoretical predictions given by the $M \rightarrow \infty$ limit (App. C.1) and the AFM (App. C.2). As is clear, we observe that the AFM approximation starts to well-describe the empirical distribution at relatively low values of M . Notice that, in the unsupervised setting, the empirical spectral distribution is characterized by two separate bulks, rather than a δ -peak and a continuous distribution: both the approximation derived in the big data limit and within AFM fails in describing this peculiarity. In Figs. 18 and 19 we reported the results for different values of ρ^2 and θ^2 . In the former, we can see that, increasing ρ with the other parameters fixed (that is, increasing the variance of the $\chi_i^{\mu,A}$ variables), the bulk approximated by a δ becomes wider, and both the approximations do not work anymore. Conversely, increasing θ has no such effect as expected. In our opinion, it is worthy to inspect the origin of the secondary bulk, however this falls outside the scope of the present paper, hence we cease to give further details on this.

D Frobenius norm and squared error

We start recalling the definition of the Frobenius Norm $\|\cdot\|_F$:

Definition 6. Let \mathbf{A} be a $N \times N$ real matrix. The (normalized) Frobenius norm of \mathbf{A} , is defined as:

$$\|\mathbf{A}\|_F := \sqrt{\frac{1}{N} \sum_{i=1}^N \sum_{j=1}^N A_{i,j}^2}. \quad (\text{D.1})$$

We recall some useful properties of the Frobenius norm (see e.g. [49]):

1. $\|\cdot\|_F$ is a matrix norm;

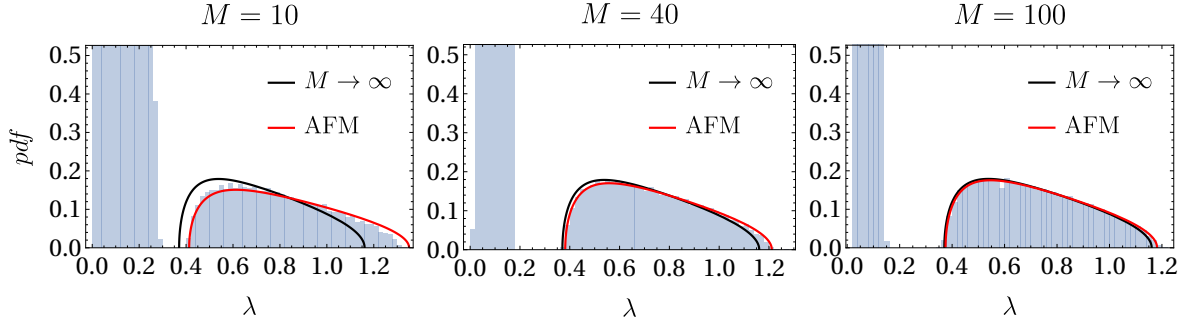


Figure 17. Histogram of the spectral distribution of \mathbf{S} with Gaussian entries, when $N = 1000$, $\alpha = 0.1$, $\theta = 0.5$, $r = 0.5$, $\rho = 0.75$, for different values of M , against the analytical formula obtained through the $M \rightarrow \infty$ approximation (black) and the AFM (red). The empirical distribution is realized by collecting the eigenvalues of a sample of 100 different realizations of the Hebbian matrices.

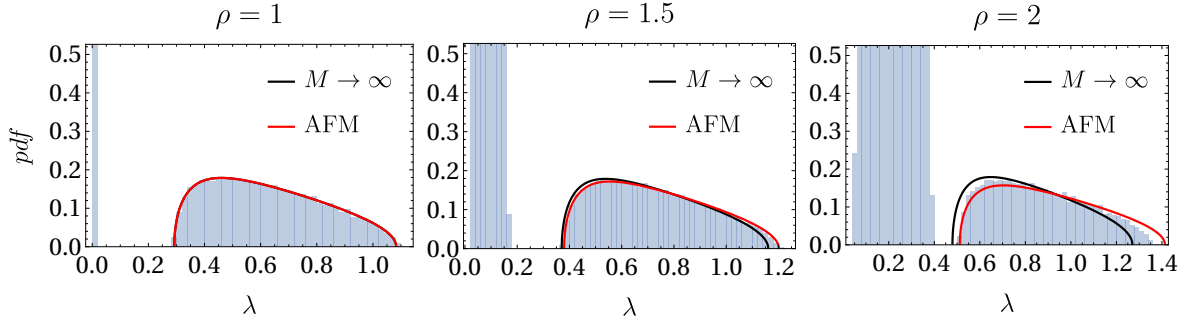


Figure 18. Histogram of the spectral distribution of \mathbf{S} with Gaussian entries, when $N = 1000$, $\alpha = 0.1$, $\theta = 0.25$, $r = 1$, $M = 50$, for different values of ρ , against the analytical formula obtained through the $M \rightarrow \infty$ approximation (black) and the AFM (red). The empirical distribution is realized by collecting the eigenvalues of a sample of 100 different realizations of the Hebbian matrices.

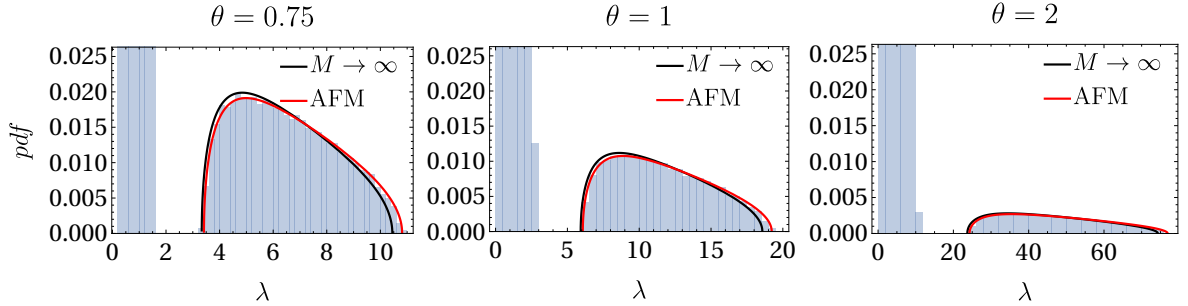


Figure 19. Histogram of the spectral distribution of \mathbf{S} with Gaussian entries, when $N = 1000$, $\alpha = 0.1$, $\rho = 1.25$, $r = 1$, $M = 50$, for different values of θ , against the analytical formula obtained through the $M \rightarrow \infty$ approximation (black) and the AFM (red). The empirical distribution is realized by collecting the eigenvalues of a sample of 100 different realizations of the Hebbian matrices.

2. $\|\cdot\|_F$ is sub-multiplicative norm, thus, given two $N \times N$ real matrices \mathbf{A} and \mathbf{B} , we have

$$\|\mathbf{AB}\|_F \leq \|\mathbf{A}\|_F \|\mathbf{B}\|_F. \quad (\text{D.2})$$

3. Given a $N \times N$ real matrix \mathbf{A} , we have that

$$\|\mathbf{A}\|_F = \sqrt{\frac{1}{N} \text{Tr}(\mathbf{AA}^T)} = \sqrt{\frac{1}{N} \sum_{i=1}^N \lambda_i^2}, \quad (\text{D.3})$$

where λ_i , $i = 1, \dots, N$, are the N eigenvalues of \mathbf{A} .

The first two properties guarantee that $\|\cdot\|_F$ is a useful norm and then can be used to induce a matrix distance. The third one, explains why we have chosen exactly the Frobenius norm, i.e. because it exploits the spectral properties of the matrix which it measures. More precisely, if we take a symmetric random matrix, in the $N \rightarrow \infty$ limit we get

$$\|\mathbf{A}\|_F = \sqrt{\frac{1}{N} \sum_{i=1}^N \lambda_i^2} \xrightarrow{N \rightarrow \infty} \sqrt{\mathbb{E}[\lambda_{\mathbf{A}}^2]},$$

where with $\lambda_{\mathbf{A}}$ we denote a stochastic variable distributed according to the limit of the empirical distribution of the eigenvalues of \mathbf{A} .

D.1 Γ^s vs Γ : the validity of supervised Hebb's rule

In order to evaluate $\mathcal{E}(\Gamma^s, \Gamma)$ it is convenient to write explicitly the difference between Γ and Γ^s

$$\Gamma_{i,j} - \Gamma_{i,j}^s = \frac{1}{N} \sum_{\mu=1}^K (1 - \bar{\chi}_i^\mu \bar{\chi}_j^\mu) \xi_i^\mu \xi_j^\mu, \quad (\text{D.4})$$

with $\bar{\chi}_i^\mu = \frac{1}{M} \sum_{A=1}^M \chi_i^{\mu,A}$. In the same spirit as the AFM, we now consider a class of i.i.d. random variables $\{\phi_i^\mu\}_{\mu,i}$, such that

$$\phi_i^\mu \phi_j^\mu = 1 - \bar{\chi}_i^\mu \bar{\chi}_j^\mu \quad \forall i \neq j, \quad (\text{D.5})$$

and with the factors ϕ_i^μ depending on the errors $\chi_i^{\mu,A}$, but not on the concepts ξ_i^μ . Then, we rewrite the difference between the two matrices in the usual form

$$\Gamma_{i,j} - \Gamma_{i,j}^s = \frac{1}{N} \sum_{\mu=1}^K (\phi_i^\mu \xi_i^\mu) (\phi_j^\mu \xi_j^\mu) + \frac{1}{N} \sum_{\mu=1}^K (1 - (\bar{\chi}_i^\mu)^2 - (\bar{\phi}_i^\mu)^2) \delta_{i,j}, \quad (\text{D.6})$$

namely, the sum of a Wishart Matrix and diagonal one. The latter in the thermodynamic limit simplifies by virtue of the strong law of large numbers, and the diagonal entries converge to a constant. Specifically

$$\alpha \frac{1}{K} \sum_{\mu=1}^K (1 - (\bar{\chi}_i^\mu)^2 - (\bar{\phi}_i^\mu)^2) \rightarrow \alpha (1 - \mathbb{E}[(\bar{\chi}_i^\mu)^2] - \mathbb{E}[(\bar{\phi}_i^\mu)^2]) := s_-^s. \quad (\text{D.7})$$

In order to compute s_-^s , we have at first to compute the second moments of the ϕ_i^μ . Recalling that $\alpha \mathbb{E}[(\xi_i^\mu)^2] = \sigma^s$ (given by Eq. (3.7)), we proceed again as follows:

$$\begin{aligned} \mathbb{E}[(\phi_i^\mu)^2]^2 &= \mathbb{E}[(\phi_i^\mu \phi_j^\mu)^2] = \mathbb{E}[(1 - \bar{\chi}_i^\mu \bar{\chi}_j^\mu)^2] = 1 - 2(1-d)^2 r^2 + \mathbb{E}[(\bar{\chi}_i^\mu)^2]^2 = \\ &= 1 - 2(1-d)^2 r^2 + (\sigma^s)^2 \\ &= 1 - 2(1-d)^2 r^2 + \left((1-d)^2 r^2 + (1-d) \frac{1 - (1-d)r^2}{M} \right)^2, \end{aligned}$$

thus

$$\begin{aligned}\sigma_-^s &:= \mathbb{E}[(\phi_i^\mu)^2] = \sqrt{1 - 2(1-d)^2 r^2 + (\sigma^s)^2} \\ &= \sqrt{1 - 2(1-d)^2 r^2 + \left((1-d)^2 r^2 + (1-d) \frac{1 - (1-d)r^2}{M} \right)^2}.\end{aligned}$$

We immediately have that

$$s_-^s = \alpha(1 - \sigma^s - \sigma_-^s). \quad (\text{D.8})$$

Concerning the contribution involving the Wishart matrix, we have $\mathbb{E}[\phi_i^\mu \xi_i^\mu] = \mathbb{E}[\phi_i^\mu] \mathbb{E}[\xi_i^\mu] = 0$, while $\mathbb{E}[(\phi_i^\mu \xi_i^\mu)^2] = \mathbb{E}[(\phi_i^\mu)^2] = \sigma_-^s$, since $\xi_i^\mu = \pm 1$. Consequently, also in this approximation the spectrum of $\mathbf{\Gamma} - \mathbf{\Gamma}^s$ is described asymptotically by a shifted Marchenko-Pastur distribution, namely $MP(\alpha, \alpha\sigma_-^s, s_-^s)$, i.e. they have the same probability distribution as $\alpha\sigma_-^s\lambda + s_-^s$, where λ follows a $MP(\alpha, 1)$ distribution. In the end, we can conclude that

$$\begin{aligned}\mathcal{E}(\mathbf{\Gamma}^s, \mathbf{\Gamma}) &= \kappa^2(\alpha, \sigma_-^s, s_-^s) = \\ &= \alpha[1 - 2(1-d)^2 r^2 + (\sigma^s)^2 + 2\alpha(\sigma^s - 1)^2] = \\ &= \alpha[1 - 2(1-d)^2 r^2 + (1-d)^4 r^4 (1+\rho)^2 + 2\alpha((1-d)^2 r^2 (1+\rho) - 1)^2],\end{aligned} \quad (\text{D.9})$$

where $\kappa^2(\alpha, \sigma^2, s)$ represents the second moment of a $MP(\alpha, \alpha\sigma^2, s)$, see Def. 5.

D.2 $\mathbf{\Gamma}^u$ vs $\mathbf{\Gamma}$: the validity of unsupervised Hebb's rule

We now focus on the squared error $\mathcal{E}(\mathbf{\Gamma}^u, \mathbf{\Gamma})$ between the basic storing coupling matrix $\mathbf{\Gamma}$ and its unsupervised counterpart $\mathbf{\Gamma}^u$. Let us rewrite the difference as

$$\Gamma_{i,j}^u - \Gamma_{i,j} = \frac{1}{N} \sum_{\mu=1}^K \left(1 - \frac{1}{M} \sum_{A=1}^M \chi_i^{\mu,A} \chi_j^{\mu,A} \right) \xi_i^\mu \xi_j^\mu. \quad (\text{D.10})$$

Adopting the AFM, we then introduce a class of i.i.d. random variables $\{\phi_i^\mu\}_{\mu,i}$ such that, for $i \neq j$, we make the following replacement:

$$1 - \frac{1}{M} \sum_{A=1}^M \chi_i^{\mu,A} \chi_j^{\mu,A} = \phi_i^\mu \phi_j^\mu. \quad (\text{D.11})$$

Again, these random variables are independent on ξ_i^μ as they only depends on the χ_i^μ . Then, we can recast (D.10) as

$$\Gamma_{i,j} - \Gamma_{i,j}^u = \frac{1}{N} \sum_{\mu=1}^K (\phi_i^\mu \xi_i^\mu)(\phi_j^\mu \xi_j^\mu) + \delta_{i,j} \frac{\alpha}{K} \sum_{\mu} (1 - (\chi_i^{\mu,A})^2 - (\phi_i^\mu)^2). \quad (\text{D.12})$$

Needless to say, this is again the sum of a Wishart Matrix and a diagonal one. Moreover, focusing on the covariance matrix and thanks to the statistical independence, we have that $\mathbb{E}[\phi_i^\mu \xi_i^\mu] = \mathbb{E}[\phi_i^\mu] \mathbb{E}[\xi_i^\mu] = 0$ and $\mathbb{E}[(\phi_i^\mu \xi_i^\mu)^2] = \mathbb{E}[(\phi_i^\mu)^2]$. As a consequence of the AFM, the spectrum of $\mathbf{\Gamma} - \mathbf{\Gamma}^u$ will follow again a Marchenko-Pastur distribution shifted by some parameter to be determined. In the thermodynamic limit by virtue of strong law of large numbers we have

$$\frac{\alpha}{K} \sum_{\mu} (1 - (\chi_i^{\mu,A})^2 - (\phi_i^\mu)^2) \rightarrow \alpha(d - \mathbb{E}[(\phi_i^\mu)^2]) := s_-^u. \quad (\text{D.13})$$

Thus, again the scale parameter and the shift of the distribution depends on the second moment of the ϕ_i^μ . This reads as

$$\begin{aligned}
\sigma_-^u &:= \mathbb{E}[(\phi_i^\mu)^2] = \sqrt{\mathbb{E}[(\phi_i^\mu \phi_j^\mu)^2]} = \sqrt{\mathbb{E}\left[\left(1 - \frac{1}{M} \sum_{A=1}^M \chi_i^{\mu,A} \chi_j^{\mu,A}\right)^2\right]} = \\
&= \sqrt{1 - 2\mathbb{E}[(\chi_i^{\mu,A})^2] + \mathbb{E}\left[\left(\frac{1}{M} \sum_{A=1}^M \chi_i^{\mu,A} \chi_j^{\mu,A}\right)^2\right]} = \\
&= \sqrt{1 - 2(1-d)^2 r^2 + (\sigma^u)^2}, \tag{D.14}
\end{aligned}$$

where σ^u is defined as in Eq. (3.12). Combining Eqs. (D.14) and (D.14), we get

$$s_-^u = \alpha (d - \sigma_-^u). \tag{D.15}$$

This implies that the limiting spectral distribution of the ensemble of matrices $\Gamma^u - \mathbf{\Gamma}$ is a shifted Marchenko-Pastur distribution $MP(\alpha, \alpha\sigma_-^u, s_-^u)$. After these considerations, we arrive to the conclusion that

$$\begin{aligned}
\mathcal{E}(\Gamma^u, \mathbf{\Gamma}) &= \kappa^2(\alpha, \sigma_-^u, s_-^u) \\
&= \alpha[1 - 2(1-d)^2 r^2 + (\sigma^u)^2 + \alpha d^2] \\
&= \alpha\left(1 - 2(1-d)^2 r^2 + (1-d)^4 r^4 + (1-d)^2 \frac{1 - (1-d)^2 r^4}{M} + \alpha d^2\right). \tag{D.16}
\end{aligned}$$

This analytical result highlights that $\mathcal{E}(\Gamma^u, \mathbf{\Gamma})$ is decreasing in r, M , increasing in d . The dependence on M and r is intuitive, because as M or r grow the dataset $\{\boldsymbol{\eta}^{\mu,A}\}_{\mu=1,\dots,K}^{A=1,\dots,M}$ gets more and more informative on the archetypes $\{\boldsymbol{\xi}^\mu\}_{\mu=1,\dots,K}$, in such a way that Γ^u provides a better approximation of $\mathbf{\Gamma}$. The role of the dilution parameter d is discussed in Sec. 5. Moreover, by deriving in α we get

$$\frac{d}{d\alpha} \mathcal{E}(\Gamma^u, \mathbf{\Gamma}) = (2d) \cdot \alpha + k(r, d, M), \tag{D.17}$$

having posed $k(r, d, M) = 1 - 2(1-d)^2 r^2 + (1-d)^4 r^4 + (1-d)^2 \frac{1 - (1-d)^2 r^4}{M}$. Therefore, we can state that for $d > 0$ there is a quadratic dependence on α , while the dependence becomes linear when $d = 0$.

E A comparison with signal-to-noise analysis

In this appendix, we relate and compare the approach developed in the present paper (and the work [42]) with a standard, non-rigorous technique used to anticipate the stability of a certain configuration and referred to as *signal-to-noise* [45] (SNA). For simplicity and without loss of generality, we will focus in this case on the stability of patterns (also referred to as *invariance*) in the unsupervised setting; specifically, the configuration $\boldsymbol{\sigma}^{(0)} = \boldsymbol{\xi}^1$ is provided as the initial condition for the neural dynamics (2.1), corresponding to $p = 1$ in the attractiveness analysis as defined in Sec. 5. Denoting with $h_i(\boldsymbol{\sigma}) = \sum_{j \neq i} \Gamma_{i,j} \sigma_j$ the local field acting on the i -th neuron, we say that the pattern $\boldsymbol{\xi}^1$ is stable under the dynamics (2.1) iff $\Delta_i(\boldsymbol{\xi}^1) = h_i(\boldsymbol{\xi}^1) \xi_i^1 > 0$ for $i = 1, \dots, N$. The basic idea in signal-to-noise analysis is to split Δ_i into a sum of signal and noise, namely positive non-random terms from stochastic contributions responsible for driving the neural dynamics away from the desired target. For instance, in the usual Hopfield model the stability of a given pattern $\boldsymbol{\xi}^1$ can be written

as $\Delta_i = \xi_i^1 \sum_{j \neq i} \Gamma_{i,j} \xi_j^1 = \sum_{j \neq i} \xi_i^1 \left(\frac{1}{N} \xi_i^1 \xi_j^1 \right) \xi_j^1 + \sum_{j \neq i} \xi_i^1 \left(\frac{1}{N} \sum_{\mu > 1} \xi_i^\mu \xi_j^\mu \right) \xi_j^1$, with the first contribution being of order 1, while the second one being the sum of uncorrelated random variables, namely a random walk of $(K-1)(N-1)$ steps with equally probable unitary jumps, see [45]. Hence, for large networks the pattern stability can be effectively approximated as $\Delta_i = S + Rz_i$, with $z_i \sim \mathcal{N}(0, 1)$. It is worth noticing that the randomness of the variables \mathbf{z} encodes the variability in the pattern stability due to all possible realizations of the patterns ξ^μ themselves, so that $\mathbb{E}_{\mathbf{z}} \equiv \mathbb{E}_{\xi}$ for large N . This implies that the signal and the noise precisely capture the first and second moments of the stability Δ_i , specifically $S = \mathbb{E}_{\xi} \Delta_i$ and $R = \mathbb{E}_{\xi} (\Delta_i^2) - S^2$. Further, whether the signal-to-noise ratio (SNR) is low ($S/R \ll 1$), the stability criterion $h_i(\xi^1) \xi_i^1 > 0$ holds for all $i = 1, \dots, N$ with large probability. Conversely, if $S/R = \mathcal{O}(1)$, the probability to have a misaligned field h_i w.r.t. the pattern is non-negligible, and neural dynamics can drive the system away from the target ξ^1 . In probabilistic terms, $\mathcal{P}(\Delta_i \geq 0) \equiv P(S + Rz_i \geq 0) = \frac{1}{2} [1 + \text{erf}(\frac{S}{\sqrt{2R^2}})]$, which matches the expression from our spectral approach within the Gaussian approximation (Def. 4) upon identifying $S = \mathbb{E}_{\xi} \Delta_i = \mu_1$ and $R^2 = \mathbb{E}_{\xi} (\Delta_i^2) - S^2 = \mu_2 - \mu_1^2$, see also [42]. In the unsupervised diluted setting, the pattern stability reads as $\Delta_i(\xi^1) = \sum_j \Gamma_{i,j}^u \xi_i^1 \xi_j^1$, and in Fig. 20, we reported the related histograms for various values of the dilution parameter, also reporting in the insets the frequency of events with $\Delta_i \geq 0$.

To analyze these results on a theoretical level, we proceed as in the usual Hopfield model splitting the pattern stability as

$$\Delta_i(\xi^1) = \sum_j \left(\frac{1}{NM} \sum_A \chi_i^{1,A} \chi_j^{1,A} \xi_i^1 \xi_j^1 \right) \xi_i^1 \xi_j^1 + \sum_j \left(\frac{1}{NM} \sum_{A, \mu > 1} \chi_i^{\mu,A} \chi_j^{\mu,A} \xi_i^\mu \xi_j^\mu \right) \xi_i^1 \xi_j^1, \quad (\text{E.1})$$

where we separated the contribution of the pattern ξ^1 to the unsupervised coupling matrix Γ^u from those of the remaining $K-1$ ground-truths. Since in our approach we included self-interactions (namely, $\Gamma_{i,i}^u \neq 0$), finite contributions to the signal can come also from the second term (this is clear by setting $i = j$ in the second quantity on the r.h.s.).¹⁴ Indeed, the terms making up the signal involve essentially the contributions of the coupling matrix due to examples at different spin sites (i, j) but belonging to the same pattern (of the form $\chi_i^{1,A} \chi_j^{1,A}$, giving contribution of order $(1-d)^2$ due to statistical independence) *and* the diagonal entries of Γ^u coming from all of the ground-truths (thus involving terms of the form $(\chi_i^{\mu,A})^2$, whose magnitude is tuned by $1-d$). Conversely, the noise term will only receive contributions from uncorrelated pixels of the non-retrieved patterns (namely, $\chi_i^{\mu,A} \chi_j^{\mu,A}$ for $\mu > 1$ and $i \neq j$), thus the factor R will be of the order $1-d$ (i.e. the variance is of the order $(1-d)^2$). From this naive analysis, it is clear that first and second moments of the empirical spectral distribution will behave differently in terms of the dilution parameter. A cursory look at the histograms in Fig. 20 confirms this expectations, as the general effect of dilution is to reduce both the signal (the mean) and the noise (the variance) of the pattern stability. Indeed, at low α and without dilution, the majority of the Δ_i are strictly positive, and increasing d results in a simultaneous shift of the empirical distribution towards zero values and a drastic suppression of the variance; in this case, a higher d results in a higher spin-flip chance (corresponding to $\Delta_i < 0$), as also remarked by the inset in left upper plot. At higher α and zero dilution, the empirical distribution is instead very broad, resulting in a significant tail below zero. Increasing the dilution in this case results in a downsizing of the probability of observing $\Delta_i < 0$, as highlighted by the inset plot in the right histogram. This effect

¹⁴This actually holds also in the usual Hopfield model, since allowing for diagonal entries of the coupling matrix Γ would result in a higher stability of patterns, leading to a 1-step magnetization $m_1 = \text{erf}(\frac{1+\alpha}{\sqrt{2\alpha}})$, rather than $m_1 = \text{erf}(\frac{1}{\sqrt{2\alpha}})$ without self-interactions.

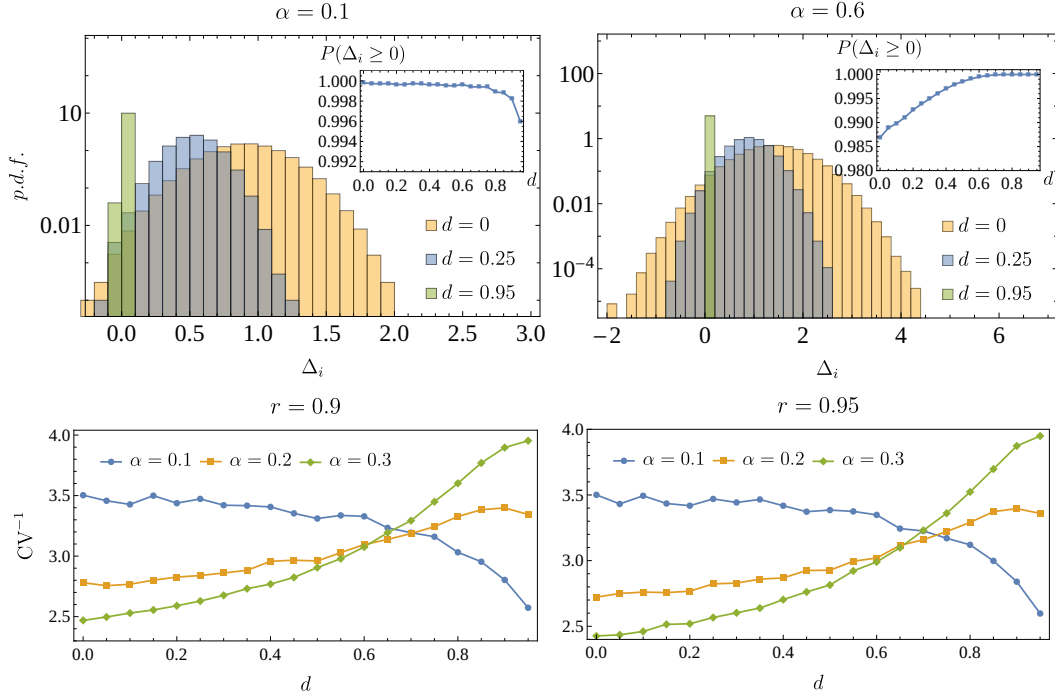


Figure 20. Details of empirical distributions of the stability in the unsupervised setting. In the first row, we reported the empirical distribution of the stability Δ_i for $\alpha = 0.1$ (left) and $\alpha = 0.6$ (right) for various values of the dilution parameters ($d = 0, 0.25, 0.95$). In the inset plots, we also reported the fraction $P(\Delta_i \geq 0)$ of events leading to positive pattern stability as a function of the dilution parameter for the same values of α . Here, $M = 50$ and $r = 0.9$. In the second row, we reported the inverse coefficient of variation (CV^{-1}) as a function of d for the empirical distributions of the pattern stability Δ_i . The plots refer to $r = 0.9$ (left) and $r = 0.95$ (right), with a storage capacity of $\alpha = 0.1$ (blue circles), 0.2 (yellow squares), 0.3 (green diamonds). The number of examples per class is $M = 50$. The results are collect by setting $\sigma^{(0)}$ to all of the ground-truths ξ^μ and computing the pattern stability, for 50 different realizations of the training dataset (and, consequently, of the coupling matrix). In both cases, the network size is $N = 1000$.

is more clear by looking at the plots in the second row of Fig. 20, where we reported the inverse of coefficient of variation (CV, which is essentially the inverse of the SNR) as a function of d for various values of α . At low α , CV^{-1} is a monotonously decreasing function of d , thus patterns are made less stable. For higher storage (above the threshold $\alpha_c = 0.14$), diluting the training set is beneficial, and the argument of the error function will increase, thus signaling better stability performances (in terms of the 1-step magnetization m_1). To conclude, we can perform a standard signal-to-noise analysis for the pattern stability $\Delta_i(\xi^1)$ in the large N limit, with the working hypothesis that isolated contributions in Eq. (E.1) are mutually uncorrelated. In particular, it is easy to verify that

$$\sum_j \left(\frac{1}{NM} \sum_A \chi_i^{1,A} \chi_j^{1,A} \xi_i^1 \xi_j^1 \right) \xi_i^1 \xi_j^1 \sim r^2 (1-d)^2 + \mathcal{O}(N^{-1/2}),$$

while

$$\sum_j \left(\frac{1}{NM} \sum_{A,\mu>1} \chi_i^{\mu,A} \chi_j^{\mu,A} \xi_i^\mu \xi_j^\mu \right) \xi_i^1 \xi_j^1 \sim \alpha(1-d) + \sqrt{\frac{\alpha(1-d)^2}{M}} z_i,$$

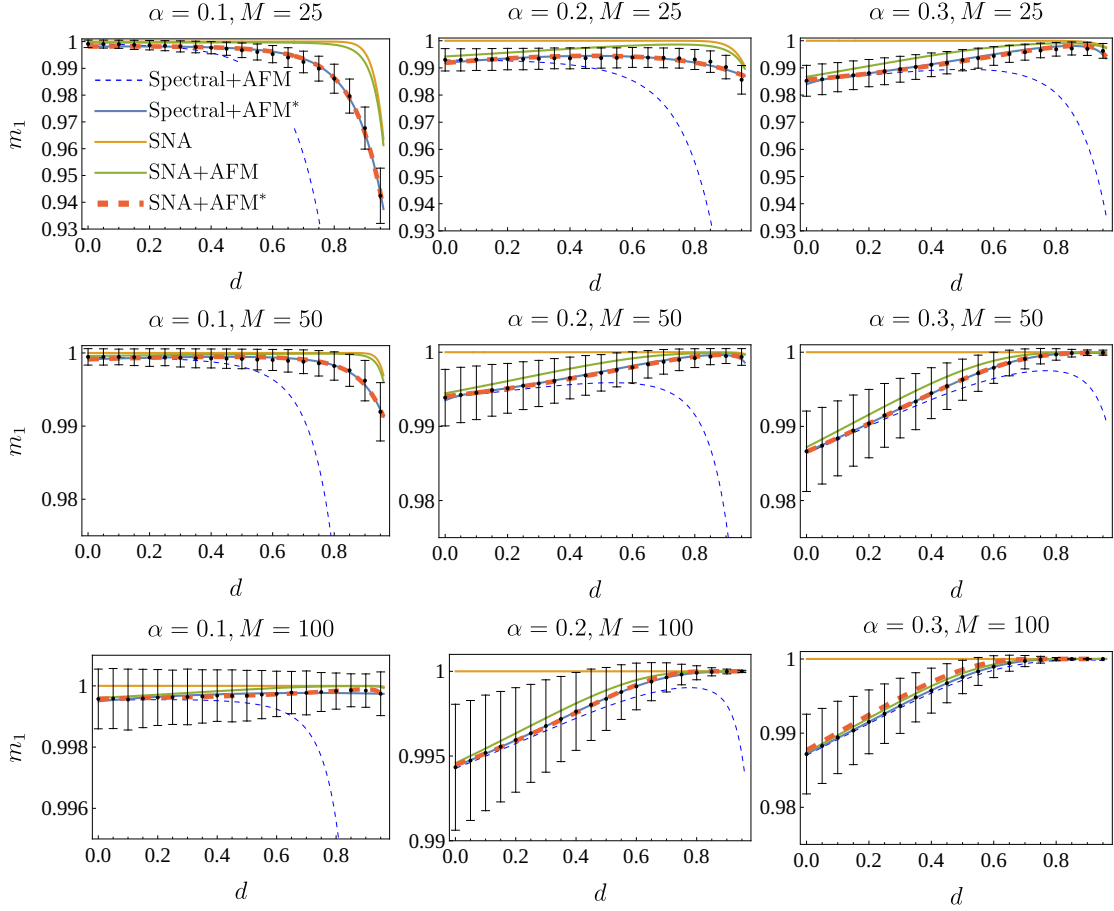


Figure 21. Comparison between signal-to-noise and spectral approach. The plots report the empirical results for the 1-step magnetization m_1 as a function of d (black markers) compared to five different theoretical predictions: spectral approach with AFM (Spectral+AFM, dashed blue line), the best-fitting version of the theoretical prediction of the spectral approach with AFM (Spectral+AFM*, blue solid line), the naive SNR (SNR, yellow curve), SNR+AFM (SNR+AFM, green curve), and the best-fitting version of SNR+AFM (SNR+AFM*, dashed thick red line). The nine plots refer to $\alpha = 0.1, 0.2, 0.3$ (from left to right), and $M = 25, 50, 100$ (from top to bottom). The empirical results at $r = 0.9$ averaging over 50 different realizations of the training dataset (and, consequently, of the coupling matrix). The network size is $N = 1000$.

where again $z_i \sim \mathcal{N}(0, 1)$. Thus, clearly $S \equiv \mathbb{E}_z \Delta_i = r^2(1-d)^2 + \alpha(1-d)$ and $R^2 \equiv \mathbb{E}_z \Delta_i^2 - S^2 = \alpha M^{-1}(1-d)^2$. If the Δ_i at different spin site are independent, we can still approximate $m_1 = 2\mathcal{P}(\Delta_i \geq 0) - 1 = \text{erf}(S/\sqrt{2R^2})$. This naive signal-to-noise analysis results in the same expression of the signal if compared to the spectral approach with the AFM, but fails in evaluating the second moment, as it gives a poor estimation of the noise (in particular, it is independent on r). We can improve this analysis by means of AFM

$$\frac{1}{M} \sum_{A=1}^M \chi_i^{\mu,A} \chi_j^{\mu,A} \approx \phi_i^\mu \phi_j^\mu,$$

for $i \neq j$. This procedure leads to the same signal $S = \alpha(1-d) + r^2(1-d)^2$, and a better evaluation

of the noise, which reads as

$$R \approx \sqrt{\alpha \left((1-d)^4 r^4 + (1-d)^2 \frac{1 - (1-d)^2 r^4}{M} \right)}.$$

This expression reproduces the one provided by naive SNA only for $r = 0$, thus signaling that the latter only works for totally uncorrelated examples. The comparison between the numerical experiments and the theoretical predictions are reported in Fig. 21, where we reported the 1-step magnetization in five different settings: naive signal-to-noise (SNA), signal-to-noise with AFM (SNA+AFM and SNA+AFM*, *vide infra*), spectral approach with AFM (Spectral+AFM and Spectral+AFM*, again *vide infra*). SNA (yellow curve) and spectral-AFM (blue dashed line) fail in reproducing empirical data (black markers), while SNA+AFM properly working for sufficiently high M and α . However, as we also did in the main text, whenever AFM is used we can take the functional form of the theoretical 1-step magnetization seriously and fit the empirical data (these are SNA+AFM*, dashed red curve, and Spectral+AFM*, blue solid line). In this case, we consider m_1 as a function of d and treat α , r and M as tunable parameters.¹⁵ With this procedure, both the SNR+AFM and the spectral approach matches perfectly the empirical results (with a coefficient of determination close to 1). These results hence suggests that AFM (besides making computations easier and providing an effective picture of the theory) allows to derive meaningful results capturing the (at least qualitatively correct) description of Hopfield-like networks in presence of non-trivial correlations between stored vectors.

References

- [1] R. J. Little and D. B. Rubin, *Statistical analysis with missing data*. John Wiley & Sons, 2019.
- [2] C. Shorten and T. M. Khoshgoftaar, “A survey on image data augmentation for deep learning,” *Journal of big data*, vol. 6, no. 1, pp. 1–48, 2019.
- [3] S. Y. Feng, V. Gangal, J. Wei, S. Chandar, S. Vosoughi, T. Mitamura, and E. Hovy, “A survey of data augmentation approaches for nlp,” *arXiv preprint arXiv:2105.03075*, 2021.
- [4] P. J. Huber, “Robust estimation of a location parameter,” in *Breakthroughs in statistics: Methodology and distribution*, pp. 492–518, Springer, 1992.
- [5] J. T. Barron, “A general and adaptive robust loss function,” in *Proceedings of the IEEE/CVF conference on computer vision and pattern recognition*, pp. 4331–4339, 2019.
- [6] L. Breiman, “Random forests,” *Machine learning*, vol. 45, pp. 5–32, 2001.
- [7] L. Prechelt, “Early stopping-but when?,” in *Neural Networks: Tricks of the trade*, pp. 55–69, Springer, 2002.
- [8] N. Srivastava, G. Hinton, A. Krizhevsky, I. Sutskever, and R. Salakhutdinov, “Dropout: a simple way to prevent neural networks from overfitting,” *The journal of machine learning research*, vol. 15, no. 1, pp. 1929–1958, 2014.
- [9] C. M. Bishop, “Training with noise is equivalent to tikhonov regularization,” *Neural computation*, vol. 7, no. 1, pp. 108–116, 1995.
- [10] I. J. Goodfellow, J. Shlens, and C. Szegedy, “Explaining and harnessing adversarial examples,” *arXiv preprint arXiv:1412.6572*, 2014.

¹⁵Clearly, α , M and r are parameters characterizing the training dataset, the best-fitting values have not physical meaning. The purpose here is to show that the theoretical predictions provided by SNR+AFM and the spectral approach have enough complexity to capture the qualitative behavior of the empirical results. For this reason, we do not report the best-fitting values for the best-fitting parameters.

- [11] T. Chen, S. Kornblith, M. Norouzi, and G. Hinton, “A simple framework for contrastive learning of visual representations,” in *International conference on machine learning*, pp. 1597–1607, PmLR, 2020.
- [12] J. Devlin, M.-W. Chang, K. Lee, and K. Toutanova, “Bert: Pre-training of deep bidirectional transformers for language understanding,” in *Proceedings of the 2019 conference of the North American chapter of the association for computational linguistics: human language technologies, volume 1 (long and short papers)*, pp. 4171–4186, 2019.
- [13] E. Agliari, F. Alemanno, A. Barra, and G. De Marzo, “The emergence of a concept in shallow neural networks,” *Neural Networks*, vol. 148, pp. 232–253, 2022.
- [14] L. Leuzzi, A. Patti, and F. Ricci-Tersenghi, “A quantitative analysis of a generalized hopfield model that stores and retrieves mismatched memory patterns,” *Journal of Statistical Mechanics: Theory and Experiment*, vol. 2022, p. 073301, aug 2022.
- [15] F. Alemanno, M. Aquaro, I. Kanter, A. Barra, and E. Agliari, “Supervised Hebbian learning,” *Europhysics Letters*, vol. 141, no. 1, p. 11001, 2023.
- [16] B. Pham, G. Raya, M. Negri, M. J. Zaki, L. Ambrogioni, and D. Krotov, “Memorization to generalization: The emergence of diffusion models from associative memory,” 2024.
- [17] M. Negri, C. Lauditi, G. Perugini, C. Lucibello, and E. M. Malatesta, “Random Features Hopfield Networks generalize retrieval to previously unseen examples,” in *Associative Memory & Hopfield Networks in 2023*, 2023.
- [18] G. Catania, A. Decelle, C. Furtlehner, and B. Seoane, “A theoretical framework for overfitting in energy-based modeling,” *arXiv preprint arXiv:2501.19158*, 2025.
- [19] J. Fontanari, “Generalization in a Hopfield network,” *Journal of Physics France*, vol. 51, pp. 2421–2430, 1990.
- [20] L. Litinskii, “Generalization in the Hopfield model,” in *IJCNN’01. International Joint Conference on Neural Networks. Proceedings (Cat. No.01CH37222)*, vol. 1, pp. 65–70 vol.1, 2001.
- [21] P. R. Krebs and W. K. Theumann, “Generalization in a hopfield network with noise,” *Journal of Physics A: Mathematical and General*, vol. 26, p. 3983, aug 1993.
- [22] E. Agliari, M. Aquaro, F. Alemanno, and A. Fachechi, “Regularization, early-stopping and dreaming: a hopfield-like setup to address generalization and overfitting,” *Neural Networks*, vol. 177, p. 106389, 2024.
- [23] A. Fachechi, E. Agliari, and A. Barra, “Dreaming neural networks: forgetting spurious memories and reinforcing pure ones,” *Neural Networks*, vol. 112, pp. 24–40, 2019.
- [24] F. E. Leonelli, E. Agliari, L. Albanese, and A. Barra, “On the effective initialisation for restricted Boltzmann machines via duality with Hopfield model,” *Neural Networks*, vol. 143, pp. 314–326, 2021.
- [25] E. Agliari, F. Alemanno, A. Barra, and G. De Marzo, “The emergence of a concept in shallow neural networks,” *Neural Networks*, vol. 148, pp. 232–253, 2022.
- [26] M. Aquaro, F. Alemanno, I. Kanter, A. Barra, and E. Agliari, “Supervised Hebbian learning,” *Europhysics Letters - Perspective*, vol. 141, p. 11001, 2023.
- [27] A. Bovier, V. Gayraud, and P. Picco, “Artificial neural networks. a review from physical and mathematical points of view,” *Annales de l’I. H. P., section A*, vol. 64, no. 3, pp. 289–307, 1996.
- [28] A. Coolen, R. Kühn, and P. Sollich, *Theory of neural information processing systems*. Oxford University Press, 2005.
- [29] T. Kohonen and M. Ruohonen, “Representation of Associated Data by Matrix Operators,” *IEEE Transactions on Computers*, 1973.

- [30] E. Gardner, “Multiconnected neural network models,” *Journal of Physics A: General Physics*, vol. 20, 1987.
- [31] A. Fachechi, E. Agliari, and A. Barra, “Dreaming neural networks: Forgetting spurious memories and reinforcing pure ones,” *Neural Networks*, vol. 112, pp. 24–40, 2019.
- [32] E. Agliari, F. Alemanno, A. Barra, and A. Fachechi, “Dreaming neural networks: rigorous results,” *Journal of Statistical Mechanics*, p. 083503, 2019.
- [33] E. Agliari, F. Alemanno, M. Aquaro, A. Barra, F. Durante, and I. Kanter, “Hebbian dreaming for small datasets,” *Neural Networks*, vol. 173, p. 106174, 2024.
- [34] D. Hebb, *The Organization of Behavior: A Neuropsychological Theory*. New York, NY: John Wiley & Sons, 1949.
- [35] J. J. Hopfield, “Neural networks and physical systems with emergent collective computational abilities,” *Proceedings of the national academy of sciences*, vol. 79, no. 8, pp. 2554–2558, 1982.
- [36] D. J. Amit, H. Gutfreund, and H. Sompolinsky, “Storing infinite numbers of patterns in a spin-glass model of neural networks,” *Physical Review Letters*, vol. 55, pp. 1530–1533, 1985.
- [37] E. Agliari, A. Barra, A. Galluzzi, F. Guerra, and F. Moauro, “Multitasking associative networks,” *Physical review letters*, vol. 109, no. 26, p. 268101, 2012.
- [38] E. Agliari, A. Barra, A. De Antoni, and A. Galluzzi, “Parallel retrieval of correlated patterns: From hopfield networks to Boltzmann machines,” *Neural Networks*, vol. 38, pp. 52–63, 2013.
- [39] E. Agliari, A. Annibale, A. Barra, A. Coolen, and D. Tantari, “Immune networks: multitasking capabilities at medium load,” *Journal of Physics A*, vol. 46, p. 335101, 2013.
- [40] E. Agliari, A. Annibale, A. Barra, A. Coolen, and D. Tantari, “Immune networks: multitasking capabilities near saturation,” *Journal of Physics A*, vol. 46, p. 415003, 2013.
- [41] E. Agliari, A. Alessandrelli, A. Barra, and F. Ricci-Tersenghi, “Parallel learning by multitasking neural networks,” *J. Stat. Mech.*, p. 113401, 2023.
- [42] E. Agliari, A. Fachechi, and D. Luongo, “A spectral approach to Hebbian-like neural networks,” *Applied Mathematics and Computation*, vol. 474, p. 128689, 2024.
- [43] J. Bernstein, A. Vahdat, Y. Yue, and M.-Y. Liu, “On the distance between two neural networks and the stability of learning,” *Advances in Neural Information Processing Systems*, vol. 33, pp. 21370–21381, 2020.
- [44] M. Benedetti, L. Carillo, E. Marinari, and M. Mézard, “Eigenvector dreaming,” *Journal of Statistical Mechanics: Theory and Experiment*, vol. 2024, no. 1, p. 013302, 2024.
- [45] D. Amit, *Modeling brain function: The world of attractor neural networks*. Cambridge university press, 1989.
- [46] R. McEliece, E. Posner, E. Rodemich, and S. Venkatesh, “The capacity of the hopfield associative memory,” *IEEE transactions on Information Theory*, vol. 33, no. 4, pp. 461–482, 1987.
- [47] Z. Bai and J. W. Silverstein, *Spectral analysis of large dimensional random matrices*, vol. 20. Springer, 2010.
- [48] I. Pinelis and R. Molzon, “Optimal-order bounds on the rate of convergence to normality in the multivariate delta method,” 2016.
- [49] R. A. Horn and C. R. Johnson, *Matrix analysis*. Cambridge university press, 2012.